

AMERICAN UNIVERSITY OF BEIRUT

CFD SIMULATION OF LAMINAR FLOWS IN A NOVEL
PRINTED-CIRCUIT HEAT EXCHANGER

by
SAHAR MOUSA ATAYA

A thesis
submitted in partial fulfillment of the requirements
for the degree of Master of Science
to Baha and Walid Bastane Department of Chemical Engineering and Advance Energy
of the Maroun Semaan Faculty of Engineering and Architecture
at the American University of Beirut

Beirut, Lebanon
January, 2022

AMERICAN UNIVERSITY OF BEIRUT

CFD SIMULATION OF LAMINAR FLOWS IN A NOVEL
PRINTED-CIRCUIT HEAT EXCHANGER

by
SAHAR MOUSA ATAYA

Approved by



Dr. Fouad Azizi, Associate Professor Advisor
Baha and Walid Basstane Department of Chemical
Engineering and Advanced Energy

Walid Saad



Dr. Walid Saad, Associate Professor Member of Committee
Baha and Walid Basstane Department of Chemical
Engineering and Advanced Energy



Dr. Marwan Darwish, Professor Member of Committee
Department of Mechanical Engineering



Dr. Charbel Habchi, Associate Professor Member of Committee
Department of Mechanical Engineering
Notre Dame University

Date of thesis defense: January 27, 2022

ACKNOWLEDGEMENTS

First, I'd like to thank my thesis advisor Dr. Fouad Azizi for his guidance and patience during all the stages of this research. I would also like to thank the Committee members: Dr. Marwaan Darwich, Dr. Charbel Habchi and Dr Walid Saad for the valuable advice and input they provided towards this work.

Also, I'd like to acknowledge all the staff at Baha and Walid Basstne Department of Chemical Engineering and Advance Energy as well as the Office of information Technology at the American university of Beirut for the helpful technical support they provided during this research.

ABSTRACT

OF THE THESIS OF

Sahar Mousa Ataya

for

Master of Science

Major: Chemical Engineering

Title: CFD Simulation of Laminar Flows in a Novel Printed-Circuit Heat Exchanger

To improve mixing quality and thermal homogeneity in small scale industrial applications involving viscous fluids, different microstructures have been designed. Split-and-Recombine (SAR) microstructures are one of the designs that have been extensively studied due to their compactness and efficiency.

The current work is a numerical study that describes the mixing, hydrodynamic and thermal performance of a new SAR geometry design used as a multifunctional heat exchanger. This new design utilizes double separation and recombination to achieve good mixing and heat transfer in a very compact structure. For this purpose, computational fluid dynamics tools were used to compute and assess mixing indices, pressure drop, friction factor, and thermal homogenization for a viscous fluid at different flow conditions. The findings were compared against two commonly used SAR mixers in the literature in the Reynolds range of 1 to 300. The results show that for $Re < 200$, the new Double SAR design show mixing performance comparable to Chen SAR, but superior to Gray SAR design. Beyond $Re = 200$ all the designs exhibited perfect mixing $> 99\%$. On the other hand, the thermal-hydraulic performance of the Double SAR was lower yet close to that of Gray SAR (with difference ranging between 19 % and 25%). Nonetheless, it was superior to the thermal- hydraulic performance of Chen SAR (with difference ranging between 70 % and 85%). Hence, the new Double SAR design has proved to offer a balance performance: achieving both good mixing quality and thermal homogenization at low energy expenditure.

TABLE OF CONTENTS

ACKNOWLEDGEMENTS	1
ABSTRACT	2
ILLUSTRATIONS	5
TABLES	8
Nomenclature.....	9
Introduction	12
A. Objective/Research Question.....	14
B. Layout of the Thesis.....	14
Literature Review	16
A. Effect of SAR configuration on the mixing performance and hydrodynamics	16
B. Effect of SAR configuration on the heat-transfer performance	21
Theoretical BackGround	27
A. Baker’s Transformation and SAR processes	27
B. Mixing performance.....	28
C. Hydrodynamic Performance: Pressure losses and friction factors.....	29
D. Heat Transfer in SAR configurations	31
methodology	35

A. Computational Domain.....	35
B. Mathematical Model	37
C. Working fluid	39
D. Operating Parameters and Boundary Conditions	40
E. Computational Models and Solution Methods.....	40
F. Implementation of the Computational Models in Ansys Fluent.....	42
Results and discussion	44
A. Mixing.....	44
1. Flow structure	44
2. Scalar mixing	52
B. Pressure drop and friction factor	63
C. Thermal and Hydrodynamics Analysis	69
1. Nature of heat transfer	70
2. Model Validation for the Thermal Analysis	71
3. Convective heat transfer	72
4. Numerical Analysis of heat transfer	73
APPENDIX A Richardson Extrapolation	83
Appendix B Mixing efficiency as a function of various SAR lengths.....	88
REFERENCES	93

ILLUSTRATIONS

Figure

1. SAR mixer configuration elementary units (a) Gray, (b) Chen, (c) 3-D flow (Ghanem et al., 2013b).....	17
2. Design of (a) Chain and (b) Teardrop micromixer (all dimensions are in mm) (Viktorov et al., 2015).....	18
3. Design of 3D C-H micromixer (all dimensions are in mm) (Viktorov et al., 2015).....	19
4. (a) 3D serpentine SAR micromixer (Hossain & Kim, 2015), (b) 3D serpentine micromixer (Ansari, 2009).....	19
5. Micromixer configurations: a) Gray SAR, b) Chen SAR, and c) Double SAR (C. Habchi et al., 2018).....	20
6. SAR1: a) Gray SAR geometry, b) SAR2 Chen SAR geometry.....	22
7. HEX reactors with different SAR-based configurations. (Anxionnaz-Minvielle et al., 2017).....	24
8. The geometric construction of (a) Chen, (b) Gray, (c) CLM3, and (d) CLM4 (Bahrani et al., 2019).....	25
9. The geometric construction of helical heat exchangers (a) HHE1 (b) HHE2 (Bahrani et al., 2019).....	26
10. Top: illustration of baker's transformation after two iterations. Bottom: a diagram of 3D mixing after two iterations (Carrière, 2007).....	28
11. Single elements of the flow configurations a. T-shaped mixer, b. Gray SAR, c. Chen SAR d. Double SAR.	36
12. Stream lines at Re=1, for a) Chen b) Double, c) Gray SAR geometries.....	45
13. Stream lines at Re=50, for a) Chen b) Double, c) Gray SAR geometries.....	46
14. Streamlines at Re=300, for a) Chen b) Double, c) Gray SAR geometries.....	47
15. Velocity vectors Profiles for Chen geometry for different flow regimes, a) Re=50, b) Re=300 (at the mid XY plane z=0.015m).....	48
16. Velocity vectors Profiles for Double geometry for different flow regimes, a) Re=50, and b) Re=300 (at the mid XY plane z=0.015m).....	48
17. Velocity vectors Profiles for Gray geometry for different flow regimes, a) Re=50, and b) Re=300 (at the mid XY plane z=0.015m).....	49

18. Isometric view, outlet scalar concentration and streamlines in the straight duct geometry (at the left column $Re=1$ and at the right column $Re=300$).....	50
19. Isometric view, of the scalar concentrations in a) Chen, b) Double and c) Gray SAR at $Re=1$ (left column) and $Re= 300$ (right column).....	51
20. progression of concentration SAR geometries: a) Chen SAR, b) Double SAR, and c) Gray SAR at the upper row $Re=1$ and at the lower row $Re=300$ at the outlet of each SAR element.....	52
21. Mixing index along the length of Gray geometry evaluated at the exit of every SAR element.	53
22. Mixing index at the outlet of Gray SAR as a function of various flow conditions.	55
23. Velocity profile of Double SAR at $Re=200$	55
24. mixing index along the length of Double geometry evaluated at the exit of every SAR element.....	56
25. Mixing index at the outlet of Double SAR as a function of various flow conditions	57
26. Mixing index along the length of Chen geometry evaluated at the exit of every SAR element	58
27. Mixing index at the outlet of Chen SAR as a function of various flow conditions	59
28. Mixing index vs. Re for all three SAR configurations combined and the straight duct.	60
29. Evolution of the mixing index along different lengths of the SAR configurations at $Re= 1$	62
30. Validation of the Pressure drop.....	64
31. Pressure drop across the 3 SAR geometries.....	66
32. Energy Consumption as a function of flow conditions in the 4 geometries under study	67
33. Mixing Index as a function of energy consumption.....	68
34. Normalized friction factors	69
35. Validation for Nusselt number in straight channel.....	72
36. Contours of velocity (a) and temperature (b) in Double geometry at $Re=50$...	73
37. Average Nusselt number per SAR element as a function of a) Gray, b) Chen, and c) Double SAR geometries.....	74

38. Average Nusselt number as a function of straight length in straight duct geometry.....	75
39. Relative Nusselt number vs. Reynolds number	75
40. Relation between Nusselt number and Energy Consumption.....	78
41. Thermal Enhancement Factor	79

TABLES

Table

42. Geometric Characteristics of the Configurations under study	36
43. Working fluid Properties (Anxionnaz-Minvielle et al., 2017).	39
44. Reynolds number and corresponding velocities used in the simulation	40
45. Fluent setup	41
46. Mesh size of the various geometries.	43
47. Richardson number	70

NOMENCLATURE

A_c	Cross-sectional area	[m ²]
A_s	Surface Area	[m ²]
c_0	Point concentration in the non-mixing section	[-]
c_∞	Complete mixed concentration.	[-]
c_i	Mass fraction at i^{th} sampling point in the plane,	[-]
c_i'	Point concentration,	[-]
\bar{c}_m	Maximum mixing mass fraction,	[-]
c_p	Specific heat,	[J/kg. K]
CoV	Coefficient of variation	[-]
d	Developed length	[m]
D_h	Hydraulic diameter	[m]
E	Energy	[W]
Ev	Energy consumption	[W/m ³]
f	Fanning friction factor	[-]
\vec{f}	External body force	[-]
g	Gravitational field acceleration	[m/s]
Gr	Grashof number	[-]
h	Heat transfer coefficient	[W/m ² K]
I_M	Mixing Index	[-]
k	Thermal conductivity	[W/m.K]
L	Representative dimension	[m]
L_t	total length	[m]

\dot{m}	Mass flow rate	[Kg/m ³]
N_s	Number of sampling points	[-]
N	Number of faces	[-]
Nu	Nusselt number	[-]
p	Static pressure (Pa)	[Pa]
Pr	Prandlt number.	[-]
q	Heat transfer rate	[W/m ²]
Q	Volumetric flow rate	[m ³ /s]
G_z	Graetz number	[-]
Re	Reynolds number	[-]
Ri	Richardson number	[-]
S_h	Energy from other heat sources.	[W]
S_m	The mass added to the continuous phase from the dispersed second phase.	[Kg]
T_b	The temperature of the bulk fluid	[K]
T_{in}	Inlet temperature	[K]
T_{out}	Outlet temperature	[K]
T_{lm}	Log-mean temperature difference	[K]
T_w	Wall temperature	[K]
V	Volume	[m ³]
\vec{V}	Velocity vector	[-]
u_m	Mean velocity of a fluid	[m/s]
x	Straight length	[m]
Greek Symbols		
α	Volume fraction of $u_m/2$ in SAR geometries	[-]

β	Volume fraction of $U_m/4$ for the Double SAR geometry	[-]
β'	The coefficient of volume expansion	[1/K]
ΔP	Pressure drop	[Pa]
ϕ_d	Dissipation function	[-]
μ	Dynamic Viscosity	[Pa.s]
ν	Kinematic viscosity	[m ² /s]
ρ	Fluid density	[kg/m ³]
σ_2	Variance of concentration	[-]
σ_{max}^2	Maximum variance for the fluid mixture	[-]
$\bar{\tau}$	Stress tensor	[N/m ²]

CHAPTER I

INTRODUCTION

Mixing processes are essential operations in the chemical industries (Hermann et al., 2018); their intent is to enhance the homogeneity of the system and its uniformity (Mosorov, 2015). Typically, the non-uniformity is manifested as a gradient of properties such as concentration, viscosity, temperature. (Ghotli, et al., 2013). Therefore, optimal mixing quality, thermal homogenization, and thermal performance are critical components in many engineering units, including heat exchangers, reactors, and contactors (Boukhalkhal et al., 2017). Improving these properties can be achieved via the intensification of heat and mass transfer processes within a system (Jegatheeswaran et al., 2018). Such process intensifications require the development of novel designs and methods that are expected to bring about enhancements at the production and processing levels for the related engineering application, improving compactness and performance and decreasing energy requirements and production costs. (Ali, 2015)

Mixing at small scale depends on molecular diffusion. At these levels, two different strategies are used for inducing mixing, by which micromixers can be categorized into two types, active and passive. Active designs need an external energy source to ensure flow agitation, such as irregular pumping, electric fields, electro-osmosis, small impellers (Viktorov et al., 2015, Hossain & Kim, 2015). Whereas passive designs rely on modification of the geometry of the microchannels, for example, by inducing foams, corrugated channels, blades helical elements, or wall curvature. Such changes increase the residence time and interfacial area between the fluids by creating

multiple laminations that are stretched and recombined to promote mixing by diffusion. (Ansari & Kim, 2010, Ghanem et al., 2013a)

Passive designs do not require large energy consumption; they also occupy smaller space. They are characterized by lower equipment cost, reduced maintenance requirements, and no power need except for pumping. Whereas; active micromixers are more expensive, and the difficulty in manufacturing, integrating, and operating them is higher in comparison to passive micromixers; hence the former option is often preferable for various industrial applications (Ansari & Kim, 2010, Ghanem et al., 2013a)

Static/Passive designs operate through the principle of baker's transformation, which will be discussed later in chapter III. By generating perturbations through continuous stretching and folding, chaotic flows are formed, destroying the interface between the fluids, enhancing mixing and heat transfer processes with minimal energy expenditure (Aref et al., 2017, Boukhalkhal et al., 2017). The vast majority of the micromixer designs in the last decade were designed in accordance with baker's transformation. (Meijer et al., 2009)

Passive/Static mixer designs can also be used as multifunctional heat exchangers where mixing, chemical reaction, and heat transfer can occur simultaneously within the same device. Such designs can provide many advantages, including improved reaction control and selectivity, fewer waste products, and better safety. (Konopacki et al., 2015) Using split and recombine (SAR) passive/static as multifunctional heat exchangers have proven advantageous for improved heat and mass transfer characteristics (Bahrani et al., 2019). SAR mixers essentially join the effects of flow splitting and recombination to create chaotic laminar flow within the system, which is evident by the exponential

increase in interfacial area between flow lamellae, which improves heat and mass transfer properties. (Ghanem et al., 2013a)

A. Objective/Research Question

This work aims at assessing the hydrodynamic, mixing, and heat transfer performance of a novel split and recombine (SAR) multifunctional heat exchanger using numerical simulations. Single-phase flow will be studied over a range of Reynolds numbers (1-300), and mixing will be evaluated based on the mixing index. In addition, hydrodynamic and thermal/heat transfer and performance will be investigated by studying the pressure drop, Grashof number, and Nusselt number. They help determine the power requirements, the thermal flow nature, and heat transfer.

In addition, for a better assessment of the overall performance of the novel multifunctional mixer, its performance will be compared to two of the most commonly used SAR configurations in literature, namely, the Chen and Gray SAR configurations. (Ghanem et al., 2013a)

B. Layout of the Thesis

The first chapter introduces the aim of this thesis, and presents background information about static mixing and split and recombine multifunctional heat exchangers. Chapter II adds on the latter by summarizing the previous works that utilize SAR micromixers and/or multifunctional heat exchangers, especially studies conducted with Chen and Gray SAR configurations since they are of interest to the current work.

Chapter III explains the theoretical concepts, computational techniques, and pertinent parameters utilized to assess mixing, hydrodynamic, and thermal performance.

While Chapter IV details the methodology by showing the computational models, the material properties, the operating parameters, boundary conditions, mesh generation, as well as the solution methods used in the simulations.

Chapter V presents the results and discussion section in which the results are shown and compared under different flow conditions in terms of mixing, thermal and hydrodynamic performance of the various mixers. Finally, chapter IV ends with a summary of the key conclusions and recommendations for future research.

CHAPTER II

LITERATURE REVIEW

The following chapter summarizes the current state of knowledge, according to recent literature, in regard to the mass and heat transfer processes of fluids in different SAR mixing designs. The first section will present various literature sources studying the effect of SAR configurations on mass transfer and hydrodynamic behavior and compare the degree of enhancement they provide in terms of these properties to other SAR configurations. The second section will present similar literature; however, the essence of the analysis would be the thermal efficiency enhancement that the SAR configurations offer.

A. Effect of SAR configuration on the mixing performance and hydrodynamics

Gray SAR geometry was first introduced by B.L.Gray et al. (1999) as a new integrated microfluidic system manufactured through a novel technology for the fabrication of fluidic circuits. The geometry seen in Figure 1a has proven to facilitate diffusion by increasing the contact area between two fluids by creating multiple laminations. Numerical and experimental studies conducted to test the newly manufactured geometry proved to be a good match. The research aimed to demonstrate the technology of creating multi-level structures by showcasing the novel SAR geometry. Since then, many other manufacturing methods for creating this type of mixers, and novel geometries, have been introduced. (Gray et al., 1999)

In 2004 Chen and Meiners introduced a novel microfluidic chip that, similarly to Gray's, was manufactured to create multiple laminations that increase mixing efficiency

by diffusion. The study aimed to prove that suggested compact design can achieve effective mixing under laminar conditions. Experimentally testing the efficiency of the new SAR system seen in Figure 1b showed that the mixing increases exponentially with channel length. (Chen & Meiners, 2004) Since then, Gray and Chen SAR geometries have been extensively used in the literature to compare newly proposed microfluidic mixers, as shown in the studies presented next.

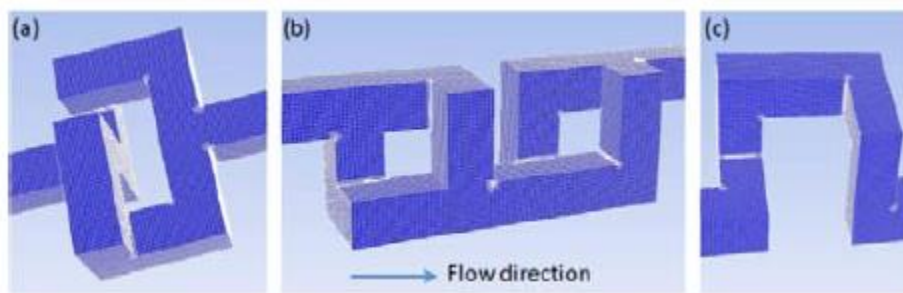


Figure 1: SAR mixer configuration elementary units (a) Gray, (b) Chen, (c) 3-D flow (Ghanem et al., 2013b)

Ghanem et al. (2013a) performed an experimental study to assess mixing and mass transfer in two SAR square duct geometries (each of 3 mm side), designed based on Gray (Figure 1a) and Chen (Figure 1b). Gray SAR consists of 48 elements spread over four parallel rows. Whereas the Chen SAR has 7 rows, each consisting of 6 elements.

Their experimental results, which were based on an assessment of the segregation indices, over a range of Reynolds number of (40-5000) showed that the Gray SAR geometry exhibited superior performance compared to the Chen SAR geometry, as optimal mixing efficiency was achieved in the former at low-Reynolds-numbers, with a short reactor length and moderate pressure losses.

respectively, of mixing indices at the exit of the 3D serpentine SAR micromixer compared to the 3D serpentine micromixer shown in Figure 4b.

Habchi et al.(2018) performed a series of CFD studies on three different SAR static mixer configurations, Gray SAR, Chen SAR, and a newly proposed Double SAR shown in Figure 5, for Reynolds numbers ranging between 0.5 and 50. The studies aimed to assess their mixing performances based on the mixing index and the overall pressure drop.

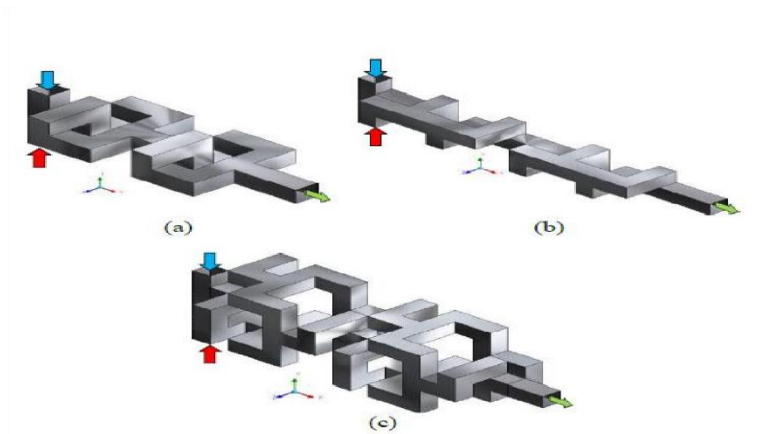


Figure 5: Micromixer configurations: a) Gray SAR, b) Chen SAR, and c) Double SAR (C. Habchi et al., 2018)

Their results demonstrated that the proposed Double SAR geometry performs better than the other two geometries at lower pressure drop. The mixing index was ~8% higher than the Chen SAR and 64% higher than the Gray geometry.

Al-Hassan et al.(2021) expanded the novel Double SAR geometry study to cover its application on viscous fluids in creeping flow regime. The geometries were larger in comparison to those used by (C. Habchi et al., 2018) and presented in Figure 5. The Gray, Chen and Double SAR geometries were composed of 12, 9 and 4 units respectively each

of 3mm side. The mixing performance was assessed for 90% glycerol-water solution over Reynolds number range of $10^{-3} \leq Re \leq 10$. The comparative analysis study concluded that the Double SAR offered better mixing performance than the other geometries under study at lower pressure drop. Hence; the Double SAR had the lower energy dissipation which amounted to be 3 times smaller than that of the Gray SAR and 4.5 times smaller than that of the Chen SAR.

B. Effect of SAR configuration on the heat-transfer performance

Ghanem et al. (2013b) performed another numerical study to assess heat transfer in the aforementioned SAR geometries and compared them to 3D-flow geometry (elementary units shown in Figure 2). The Gray, Chen, and 3-D flow geometries consist of 13, 10, and 18 units, respectively. The comparative analysis includes a 750 mm plain square duct with a hydraulic diameter of 3mm as well.

Assuming an isothermal wall, they assessed energy expenditures, overall heat transfer enhancement factor and, friction losses over a range of Reynolds number $10^{-4} \leq Re \leq 10$. As expected, the SAR geometries resulted in higher convective heat transfer. The flows in SAR configurations showed a 1,700% improvement of heat transfer efficiency over the plain square channel flow with only a moderate increase in the pressure drop. Besides, Chen SAR configuration proved to have the best heat-transfer efficiency, performing 28% better than Gray SAR and 65% better than 3-D flow geometries. Nonetheless, it witnessed the highest pressure drop in comparison and hence the highest friction factor, which amounted to a 17% increase compared to 3-D flow geometry.

Jarrahi et al. (2016) performed both experimental and numerical studies on 2 different SAR heat exchangers to examine their thermal performance under laminar flow

conditions. The heat exchangers used in the study were SAR1 and SAR2, which are modified forms of Chen and Gray SAR geometries, their elementary units are shown in Figure 6. Both geometries are composed of 8 identical units assembled in series. The temperature is constant at the shell side, and water is used on both the shell and tube sides. The studies were performed in a Reynolds number range (100-3000) when the Prandtl number is between 4.5 and 7.5.

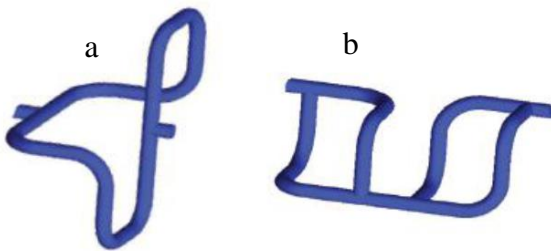


Figure 6: SAR1: a) Gray SAR geometry, b) SAR2 Chen SAR geometry

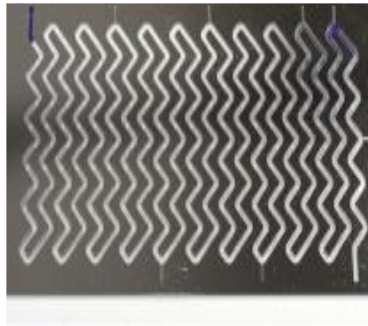
The study concluded that heat transfer in Gray SAR geometry is superior to Chen SAR's for all the flow conditions under study $100 < Re < 3000$. That conclusion is supported by the temperature profiles at the outlets, which proved to be more uniform in Gray SAR compared to Chen SAR. However, studying the heat transfer within the two geometries showed that Nusselt number and hence, the convective heat transfer in the first element of heat exchanger Gray is greater than Chen's; for the second and third elements, the Nusselt number values are very close. Nonetheless, proceeding from the first to the third element along the heat exchangers in Chen, the change in the convective heat transfer coefficient was observed to be less significant than that observed for Gray, proving that the efficiency of the former does not deteriorate as a function of the distance from the inlet for at least the first two elements. At $Re > 1500$, Nusselt number becomes

independent of Reynolds number in both configurations. Also, Gray SAR proved to be more energy-efficient than Chen SAR as it recorded lower pressure drop in comparison.

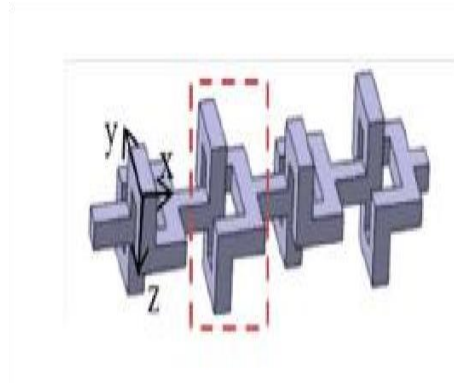
Anxionnaz-Minvielle et al. (2017) experimentally investigated the mixing performance, heat transfer, and pressure drop in the multifunctional heat exchanger shown in Figure 7, for constant wall temperature, for Reynolds numbers ranging from 0.1 to 10,000. The working fluids were selected to be distilled water, ethylene glycol, and two solutions of glycerol (70 w% and 90 w%)

The length of Gray SAR with an integrated cooling pattern is slightly more significant than the one of the Gray SAR. As expected in the low Reynolds number range ($Re < 100$), the SAR geometries enhance heat and mass transfer compared to the corrugated geometry. Also, the SAR design's energy efficiency increases in comparison to the corrugated design for more viscous fluids, especially for Reynolds numbers below 50. Integrated cooling proved unnecessary as its effect on heat transfer was very small upon comparing Gray with integrated cooling to Gray SAR geometry. Due to the higher number of splitting and recombination patterns per unit of length of the Chen geometry (+50% compared to Gray's), its heat transfer was more favorable.

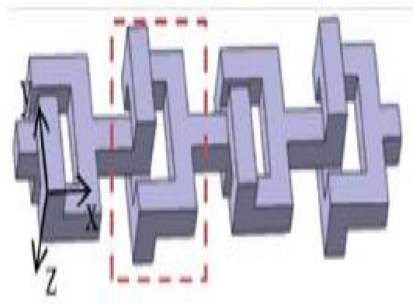
Also, it is worth noting that head losses in the corrugated geometry are higher compared to the SAR geometries. In contrast, Chen SAR geometry recorded higher head loss than Gray's due to its higher number of SAR patterns per developed length unit. (Anxionnaz-Minvielle et al., 2017)



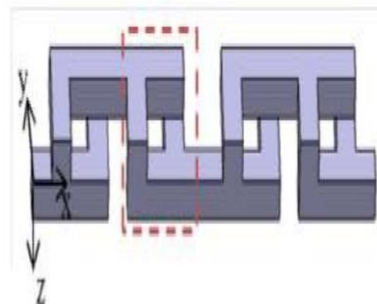
(a) corrugated channel



(b) Gray SAR with integrated cooling)



(c) Gray SAR



(d) Chen SAR

Figure 7: HEX reactors with different SAR-based configurations. (Anxionnaz-Minvielle et al., 2017)

Bahrani et al. (2019) have studied four different chaotic laminar/SAR mixers, including the Gray and Chen SAR geometries (Figure 8), and compared them to two other helical heat exchangers (Figure 9). The results show that the degree of thermal mixing improvement varies depending on the geometric construction, mainly the number of elbows and the orientation of the curvature plane.

Nusselt number values were observed to be higher in Gray and CLM3 compared to CLM4. Compared to a straight duct, the heat transfer enhancement reached more than

200% for Chen geometry, more than 400% in Gray and CLM3-4 geometries. In addition, the 4 CLM/SAR mixers have 2 times better heat transfer than the helical exchangers.

Nonetheless, the higher heat transfer performance is compensated by higher head loss. Thermal enhancement factor (discussed in chapter III) is a criterion to characterize thermal-hydraulic performance, its assessment results in concluding that except for Chen geometry, other CLM/SAR mixers have comparable performance to helical heat exchangers. Hence, Gray, CLM 3, and CLM4 are recommended for applications where the main focus is to obtain higher heat transfer. At an industrial scale, their use would be dependant on the application and its specification, given that they achieve better heat transfer performance at higher power requirements.

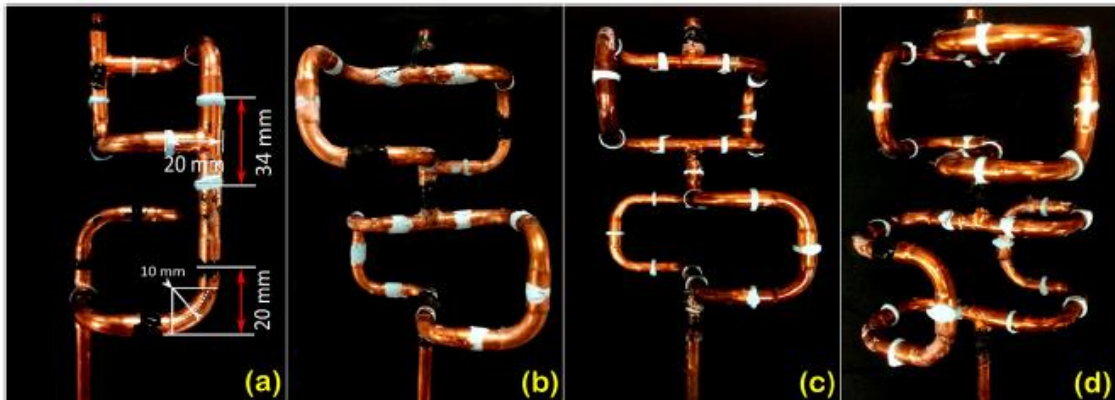


Figure 8: The geometric construction of (a) Chen, (b) Gray, (c) CLM3, and (d) CLM4 (Bahrani et al., 2019)

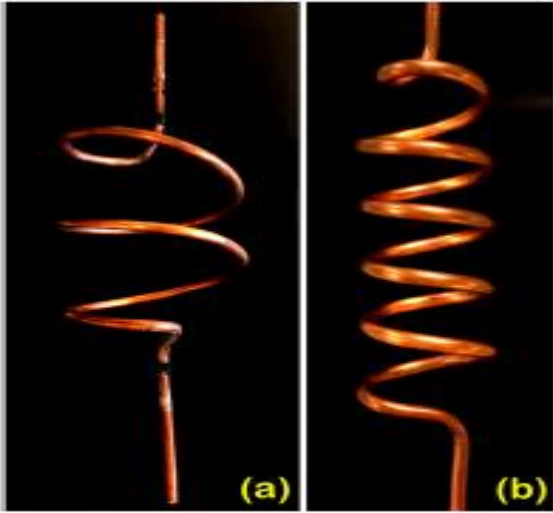


Figure 9: The geometric construction of helical heat exchangers (a) HHE1 (b) HHE2 (Bahrani et al., 2019)

CHAPTER III

THEORETICAL BACKGROUND

This chapter explains the concept behind Split and Recombine processes and the pertinent parameters used to assess and compare the mixing, hydrodynamic and thermal performance among different SAR configurations.

A. Baker's Transformation and SAR processes

To enhance mixing performance, the geometrical design is adjusted to promote secondary transverse flows (Anxionnaz-Minvielle et al., 2017; Ghanem et al., 2014). Split-and-recombine (SAR) designs modify the flow patterns which increase residence time, and hence, allow efficient mixing at lower flows rates. The streams divide, then rotate in bends, and finally recombine, achieving stretching/ squeezing diverging and the “cutting” step following the baker's transformation (Ghanem et al., 2014, Ghanem et al., 2013b) The principle of SAR processes is based on baker's transformation, illustrated in the following:

$$S(x, y) = \begin{cases} \left(2x, \frac{1}{2}y\right) & \text{if } 0 \leq x < \frac{1}{2} \\ \left(2x, \frac{1}{2}(y + 1)\right) & \text{if } \frac{1}{2} \leq x < 1 \end{cases} \quad (1)$$

“By continuously squeezing in the y -direction while stretching in the x -direction, then cutting in two and then stacking the one half above the other, multiply the two-strip domain to become four strips after one iteration. After n iterations, 2^n alternating strips of depth $1/2^n$ are obtained” as illustrated in Figure 10 (Carrière, 2007).

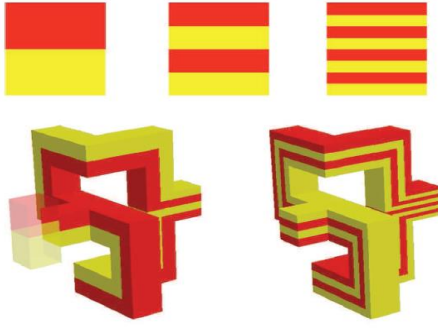


Figure 10: Top: illustration of baker's transformation after two iterations. Bottom: a diagram of 3D mixing after two iterations (Carrière, 2007)

B. Mixing performance

Different techniques can be employed to assess the mixing efficiency. One method compares the standard deviation of the point concentration in the mixing section to that in the non-mixing section (Cai et al., 2017). The mixing index, I_M is then calculated from the variance of the mass as shown in the following equations:

$$\sigma^2 = \frac{1}{N} \sum (c_i - \bar{c}_m)^2 \quad (2)$$

$$I_M = 1 - \sqrt{\frac{\sigma^2}{\sigma_{max}^2}} \quad (3)$$

Where σ^2 is the variance, c_i is the mass fraction at an i^{th} sampling point in the plane; \bar{c}_m is the maximum mixing mass fraction, N is the number of sampling points. I_M is the mixing index and σ_{max}^2 is the maximum variance for the fluid mixture. It refers to completely unmixed fluids (Ansari & Kim, 2010)

Another method is calculating the mixing index based on the comparison of the integral of the point concentration in the mixing and non-mixing sections according to the following equation:

$$I_M = 1 - \frac{\int_0^H |c_i - c_\infty| dy}{\int_0^H |c_0 - c_\infty| dy} \quad (4)$$

Where H is the width of the section, c_i is the point concentration, c_0 is the point concentration in the non-mixing section, c_∞ is the complete mixed concentration. (Cai et al., 2017)

Alternatively, using the following equation:

$$I_M = 1 - CoV = 1 - \frac{\sigma}{\bar{x}} \quad (5)$$

Where CoV is the coefficient of variation equivalent to the ratio of the standard deviation (σ) to the average scalar concentration (\bar{x}) at the outlet (Habchi et al., 2018)

C. Hydrodynamic Performance: Pressure losses and friction factors

The hydrodynamic performance of the SAR configuration in a chaotic laminar flow regime is typically investigated by means of pressure drop; since it is directly linked to the energy consumption of the mixing process. The pressure drop is usually “computed as the difference in the area-weighted average pressure between the inlet and outlet of the micromixer”. (Hossain & Kim, 2015).

The pressure drop can be linked to the fluid, the velocity, and the pipe diameter through the following equation:

$$\frac{\Delta P}{L_t} = \frac{2\rho f \times u_m^2}{D_h} \quad (6)$$

Where:

$\frac{\Delta P}{L_t}$ is the pressure drop per unit length across the multifunctional heat exchanger (Pa/m)

L_t is the total length (m)

ρ is the fluid density (kg/m³)

u_m is the average flow velocity in the straight plain pipe (m/s)

D_h is the hydraulic diameter (m)

and f is the Fanning friction factor expressed in the laminar flow regime for a square duct by the following equation:

$$f = \frac{14.227}{Re} \quad (7)$$

Where Re is the Reynolds number $Re = \frac{\rho u_m D_h}{\mu}$ (8)

and μ is the dynamic viscosity (Pa.s) (Ohkawa et al., 2008)

The Fanning friction factor is utilized to study fluid friction in pipes. It is a dimensionless number that evaluates the resistance to fluid flow at the wall. Eq 6 can be alternatively expressed as follows to represent fanning friction factor in a straight duct

$$f_{SD} = \frac{\Delta p D_h}{2L \rho u_m^2} \quad (9)$$

To apply the previous equation on a SAR configuration, estimating the friction coefficient must be weighted by the corresponding flow velocity. Due to the splitting of the flow stream in SAR geometries, the incoming velocity will be halved or even further attenuated to a quarter of the original inlet velocity in certain sections of the SAR geometry. Hence, calculating the Fanning friction coefficient requires weighing what fraction of the total volume the dominating flow velocity is equivalent to the inlet velocity, its half or its quarter.

The Fanning friction coefficient can be evaluated using the following equation by assigning α and β to the fractions of the volumes corresponding to $\frac{u_m}{2}$ and $\frac{u_m}{4}$, respectively. (Habchi, et al. 2019)

$$f_{SAR} = \frac{\Delta p D_h}{2L\rho u_m^2} (1 - \alpha - \beta) + \frac{\Delta p D_h}{2L\rho \left(\frac{u_m}{2}\right)^2} \alpha + \frac{\Delta p D_h}{2L\rho \left(\frac{u_m}{4}\right)^2} \beta \quad (10)$$

D. Heat Transfer in SAR configurations

Heat transfer in SAR configurations is often studied through Grashof number, Richardson number, and Nusselt number. The first two numbers allow the assessment of the nature of the flow, whether it is a natural or forced convection. While Nusselt number allow quantifying the extent of the convection heat transfer in numerical terms. (Shah et al., 2017)

Richardson number (Ri) characterizes the thermal stability of the flow; it is calculated according to Equation 11. (Gage & Reid, 2006, Garbrecht, 2017)

$$Ri = \frac{Gr}{Re^2} \quad (11)$$

The Grashof number (Gr) is defined as “the ratio of buoyancy to viscous forces in the boundary layer”. It allows determining the thermal flow characteristics and predicting natural and forced convection. (Rashidi et al., 2014)

The Grashof number is evaluated using the following equation:

$$Gr = \frac{g\beta'(T_w - T_b)L^3}{\nu^2} \quad (12)$$

Where

g is the gravitation field acceleration (m/s)

β' is the coefficient of volume expansion (1/K)

T_w is the temperature of the wall (K)

T_b is the temperature of the bulk fluid (K)

L is the representative dimension (m)

ν is the kinematic viscosity (m²/s) (Rashidi et al., 2014)

Natural convection is dominant when Richardson number $Ri \gg 1$; it becomes insignificant when $Ri \ll 1$; the effects of both natural and forced convection coexist and become equally effective when $Ri \cong 1$. (Garbrecht, 2017)

Higher convective heat transfer is translated into increased values of the Nusselt number. The latter is defined as “the ratio of heat transfer by convection to heat transfer by conduction under constant conditions.” (Herwig, 2016, Ghanem et al., 2013b).

Calculating Nusselt number Nu is achieved according to the following equations. (Çengel, 2011)

$$q = \dot{m}c_p(T_{out} - T_{in}) \quad (13)$$

Where:

q is the heat transfer rate (W/m²),

c_p is the specific heat (J/kg.K)

T_{in} is the inlet temperature (K)

T_{out} is outlet temperatures (K)

\dot{m} is the mass flow rate (kg/ m³) defined as,

$$\dot{m} = \rho u A_c \quad (14)$$

Where:

ρ is the fluid density (kg/m^3), u is the fluid velocity (m/s)

A_c is the cross-sectional area (m^2).

Then by utilizing Newton law for cooling, we can obtain the heat transfer coefficient h ($\text{W}/\text{m}^2\text{K}$) according to the following:

$$h = \frac{q}{AT_{lm}} = \frac{\dot{m}c_p(T_{out} - T_{in})}{AT_{lm}} \quad (15)$$

Where A is the wall surface area (m^2).

T_{lm} is the log-mean temperature difference which can be deduced using the following equation:

$$T_{lm} = \frac{(T_{in} - T_w) - (T_{out} - T_w)}{\ln \left[\frac{(T_{in} - T_w)}{(T_{out} - T_w)} \right]} \quad (16)$$

Where T_w is the wall temperature (K)

Hence Nusselt numbers can be calculated according to the following equation.

$$Nu = \frac{hD_h}{\kappa} \quad (17)$$

Where D_h is the hydraulic diameter and

κ is the thermal conductivity

To further assess the improvement of thermal efficiency, the thermal enhancement factor η is evaluated for the three SAR configurations compared to the straight duct configuration. The thermal enhancement factor η is the ratio of the surface heat transfer coefficient (h) in the SAR configuration to that of the duct configuration (h_0), at constant pumping power conditions” (Ghanem et al., 2013b)

$$\eta = \frac{h}{h_0} = \frac{N_u}{N_{u_0}} = \frac{\frac{N_u}{N_{u_0}}}{\left(\frac{f}{f_0}\right)^{\frac{1}{3}}} \quad (18)$$

CHAPTER IV

METHODOLOGY

This section provides a summary of the computational model utilized in this study. It starts with discussing the computational domain. After that, the mathematical model that constitutes the basis of the computational fluid dynamics work is presented before detailing what goes in the simulation process, starting with fluid properties, boundary conditions, operating conditions, and solution methods.

A. Computational Domain

The four configurations employed for the purpose of studying the mixing hydrodynamic and thermal performance of laminar flows in this study are Gray SAR, Chen SAR, and the new Double SAR configuration, in addition to a straight duct configuration. All the geometries were drawn using the AutoCAD drawing tool. A single element of each SAR configuration is represented in Figure 12. All geometries are equipped with 2 inlets that form a T-junction. The straight duct is a 0.654 m long duct, the Gray SAR configuration has 12 elements, and the Chen SAR micromixer consists of 9 elements, while the new Double SAR consists of 4 elements. The number of elements were chosen as such to ensure the same residence time inside each mixer.

Table 1 provides further information about the geometric characteristics of the configurations under study. It lists for each geometry the number of mixing elements, the hydraulic diameter, the total volume, cross-sectional and surface area, in addition to the straight length x , total length L_t , and developed length d .

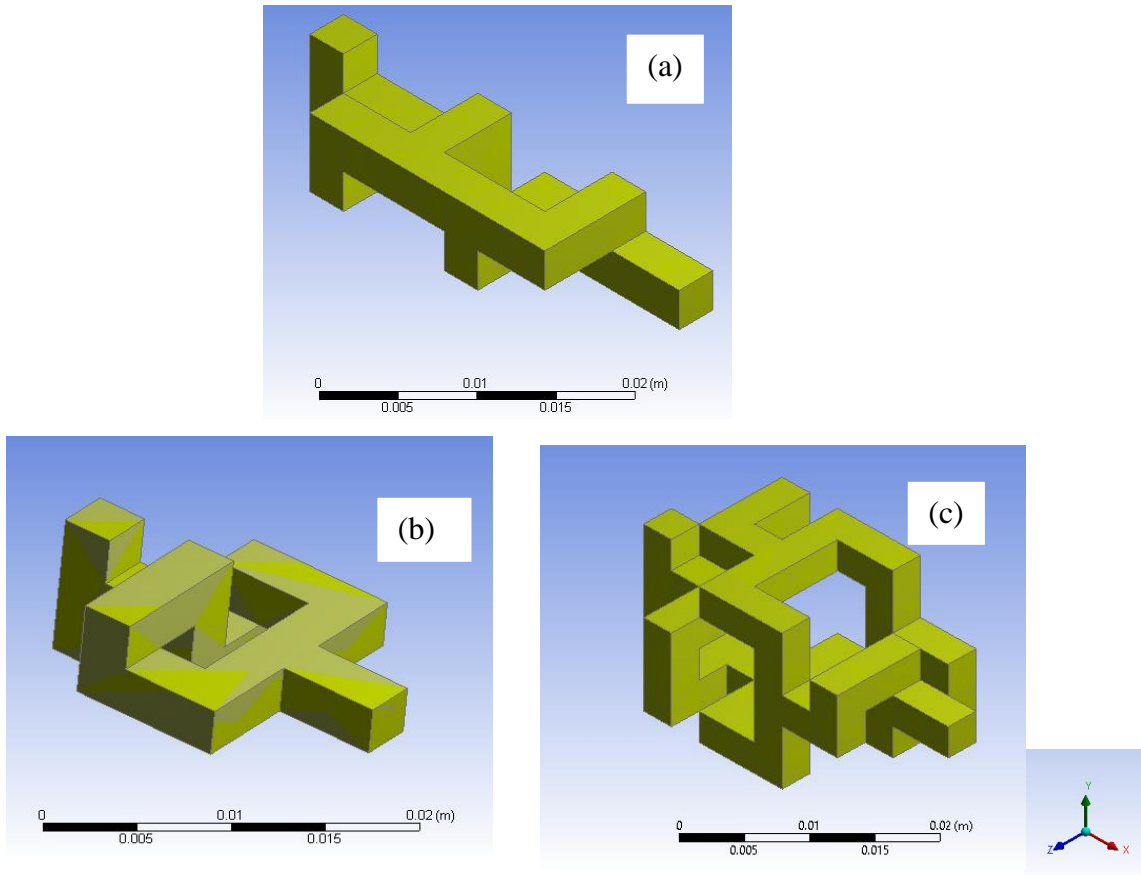


Figure 11: Single elements of the flow configurations a. T-shaped mixer, b. Gray SAR, c. Chen SAR d. Double SAR.

Table 1: Geometric Characteristics of the Configurations under study

	Straight duct	Chen SAR	Gray SAR	Double SAR
Number of elements	1	9	12	4
Hydraulic diameter (m)	0.003	0.003	0.003	0.003
Total Volume(m ³)	5.97×10^{-6}	5.7×10^{-6}	5.94×10^{-6}	5.72×10^{-6}
Total surface Area (m ²)	7.974×10^{-3}	7.290×10^{-3}	7.72×10^{-3}	7.43×10^{-3}
Straight length x (m)	0.657	0.252	0.189	0.117
Total Length L_t (m)	0.663	0.633	0.660	0.635
Developed Length d (m)	0.660	0.411	0.405	0.285

The straight length (x) is the linear distance between the inlet and the outlet. Whereas; the total length (Lt) is the “ratio of the total fluid volume divided to the cross-sectional area of the mixing channel”. On the other hand, the residence length (d) refers to the “distance covered by a fluid particle between the inlet and the outlet”. (Anxionnaz-Minvielle et al., 2017)

B. Mathematical Model

The numerical study evaluates mixing rate, pressure loss, and thermal performance. For that purpose, mass and momentum (Navier-Stokes) and energy equations are solved using finite volume approximation on a structured grid using commercial CFD code Ansys Fluent.

First, the continuity equation or the conservation of mass equation can be represented as follows:

$$\frac{\partial \rho}{\partial t} + \nabla \cdot (\rho \vec{V}) = S_m \quad (19)$$

Where S_m is the mass added to the continuous phase from the dispersed second phase (Ansys Fluent Inc, 2019).

The above formula is the general form of mass conservation equation that can be applied for both compressible and incompressible flows.

As for the momentum equation, it can be described by the following equations:

$$\frac{\partial(\rho \vec{V})}{\partial t} + \nabla \cdot (\rho \vec{V} \vec{V}) = -\nabla p + \nabla \cdot (\vec{\tau}) + \rho \vec{g} + \vec{f} \quad (20)$$

Where \vec{V} is the velocity vector

ρ is the fluid density (kg/m²)

ν is the kinematic viscosity (m²/s)

p is the static pressure (Pa)

$\bar{\tau}$ is the stress tensor (N/m²)

$\rho\vec{g}$ and \vec{f} are the gravitational body force and external body forces respectively. (Ansys Fluent Inc, 2019)

The energy equation is defined as:

$$\frac{\partial(\rho E)}{\partial t} + \nabla \cdot (\vec{V}(\rho E + p)) = \nabla \cdot \left(k_{eff} \nabla T - \sum_j h_j \vec{J}_j + (\bar{\tau} \cdot \vec{V}) \right) + S_h \quad (21)$$

Where k_{eff} is the effective conductivity, $h_j \vec{J}_j$ is the diffusion flux of species j .

On the right-hand side of the energy equation, the four terms are: energy transfer due to conduction, species diffusion, viscous dissipation, and energy from other heat sources, respectively. (Ansys Fluent Inc, 2019)

The above equations (19, 20 and 21) represent the general form Navier stokes and energy equations solved by the CFD solver. However, a simpler form of these equations can be derived by taking in consideration that gravity forces and viscous heating are neglected, and that the flow is assumed to be Newtonian, incompressible, single phase. Navier Stokes, and energy equations can be approximated as follows:

$$\nabla \cdot \vec{V} = 0 \quad (22)$$

$$(\vec{V} \cdot \nabla) \vec{V} = -\frac{1}{\rho} \nabla p + \nu \nabla^2 \vec{V} \quad (23)$$

$$\rho c_p ((\vec{V} \cdot \nabla) T) = k \nabla^2 T + \phi_d \quad (24)$$

Where c_p is the specific heat, T is the absolute temperature, and ϕ_d is the dissipation function. (R.B. Bird 2007, Juraeva & Kang, 2020)

The solution to the Navier-Stokes equation gives the velocity and pressure field for fluid flow with constant viscosity and density. In contrast, temperature and other thermal characteristics can be obtained via the solution of the energy equation.

C. Working fluid

The working fluid utilized for the purpose of this study is a water-ethylene glycol mixture (98 wt% ethylene glycol); used at temperature 300 K; its properties are listed in Table 2.

Table 2: Working fluid Properties (Anxionnaz-Minvielle et al., 2017).

98 wt% Ethylene Glycol- Water mixture	
Density (kg/m ³)	1,110
Viscosity (pa.s)	0.01
Thermal capacity (J/kg·K)	2504
Thermal conductivity (W/m.K)	0.26
Thermal diffusivity (m ² /s)	1.05×10^{-7}
Mass diffusivity(m ² /s)	2.3×10^{-13}

D. Operating Parameters and Boundary Conditions

To solve the aforementioned mathematical model, the simulations were carried out at a temperature of 300 K for Reynolds numbers 1, 10, 50, 100, 200, and 300; the velocities are hence set according to the following table:

Table 3: Reynolds number and corresponding velocities used in the simulation

Reynolds number	1	10	50	100	200	300
Inlet velocity (m/s)	1.502×10^{-3}	1.502×10^{-2}	0.075	0.150	0.300	0.450

The same model is used to carry out the thermal analysis, but in this case, the energy equation was activated, and the walls were set to a temperature of 350K. For each Reynolds number, the flow patterns are analyzed, and the pressure drop, mixing index, Nusselt, and Grashof numbers are deduced from the simulation results.

The scalar concentration value for the working fluid is set to zero (in arbitrary unit) at one inlet and 1 at the other. Same uniform velocity profiles are set at both inlets, while the outlet is set to a zero gradient pressure outlet. All the walls will be considered no-slip fixed walls, and isothermal conditions (350 K) will be assigned to solve the heat transfer simulations (Habchi et al., 2018).

E. Computational Models and Solution Methods

After assigning the fluid properties, operating parameters, and boundary conditions, the next step is to assign discretization and solution methods. Ansys Fluent solves the Navier-Stokes and energy equations finite volume method (FVM). This

method divides the domain into a number of control volumes, the variable of interest is located at their centroids. The second step is integrating the differential form of the flow equations over each control volume. (Ali, 2015)

“The simulations for the steady, incompressible flows in the multifunctional heat exchangers are solved using a double-precision, segregated, steady, implicit linearization finite-volume solver”. Since the fluid flow is incompressible and in the laminar regime and the net transport of species at inlets is predominantly diffusive, a pressure-based solver was adopted. (Ghanem et al., 2013b, Mangani et al., 2016).

As for the convergence criteria for the continuity and momentum equations, it was set at 10^{-6} , while for the energy equation it was set at 10^{-8} . Beyond these values, pressure, velocity, temperature profiles remain constant. (Ghanem et al., 2013b)

The following table summarizes the setup in fluent:

Table 4: Fluent setup

Models	Species transport	
	Energy equation	
Spatial discretization schemes	Continuity and momentum	Third order MUCSL
	Pressure	PRESTO
	Energy	Third order MUCSL

F. Implementation of the Computational Models in Ansys Fluent

The numerical computations were performed using the ANSYS Fluent 19. All the geometries detailed before were developed using AutoCAD then imported to the Design Modeler and introduced to ANSYS Meshing software to produce the CFD mesh.

CFD studies require building a grid with small enough elements that even if their size was decreased any further, the simulation will still produce similar results. Building such grid to ensure accurate results is commonly referred to as mesh sensitivity analysis. Richardson extrapolation is one of the most widely used methods for mesh sensitivity analysis in CFD since it is capable of enhancing the accuracy of a given computational technique. (Shyy et al., 2002).

The Grid Convergence Index method which is developed based on the Richardson extrapolation will be utilized in this research. (Celik et al., 2008). The method of implementation of this procedure is outlined below. It relies on developing three sets of grids the sizes of which are considerably different. For this, the grid refinement ratios should be “not too large as the grids may resolve different flow physics, also not too small as the solution changes will be very minimal and the sensitivity to grid may be difficult to identify compared to iterative errors” (Xing & Stern, 2010). Different simulations were then conducted for each grid and the mixing index, the CoV and pressure drop were calculated.

The grid convergence index GCI calculated using Richardson extrapolation can be expressed as

$$GCI_f^{21} = 1.25 \frac{|\varepsilon|}{r^p - 1} \quad (25)$$

$$\varepsilon = \frac{f_c - f_f}{f_f} \quad (26)$$

Where r and p , are the grid refinement ratio and the order of accuracy respectively.

f_c and f_f are the numerical results obtained with a courser grid and a finer grid respectively. (Celik et al., 2008; Juraeva & Kang, 2020) (For more details on Richardson extrapolation refer to Appendix A)

The sensitivity analysis was performed at the highest flow rate $Re= 300$. Once the grid satisfies the criteria of $GCI < 2.5\%$ as per Richardson extrapolation method; it would be considered adequate to be used in the simulation.

Table 2 summarizes the mesh sizes for geometries used in the simulations. All the meshes form structured hexahedral elements and are deemed to have acceptable quality with their skewness < 0.98 , aspect ratio < 50 , and orthogonal quality > 0.01 .

Table 5: Mesh size of the various geometries.

Mesh	Chen	Double	Gray	Straight duct
Number of Cells	10791827	5027871	10264320	9650550

CHAPTER V

RESULTS AND DISCUSSION

A. Mixing

This chapter presents the CFD results carried out for the flow of water-ethylene glycol mixture (98 wt. % ethylene glycol) in the 4 geometries under study. The simulations were set up as described in the previous section, and generated for Reynolds numbers of 1, 10, 50, 100, 200, and 300. The following sections will demonstrate the difference in flow behavior among the 4 configurations under the varying flow conditions and discuss the mixing and thermal efficiencies obtained for each configuration.

1. Flow structure

The behavior of the fluid under different flow conditions was examined with the aid of streamlines and velocity profiles. Figures (12-14) shows the flow streamlines for the four geometries under study for different flow conditions $Re = 1, 50$ and 300 . The fluid splits and recombine periodically in accordance to each geometrical structure, as evident by the streamlines circulates and twists along the 90 degree bends.

No swirls or vortices were observed for $Re=1$ in all the configurations however at $Re=50$ in all SAR configurations weak swirl becomes apparent and increases significantly at $Re=300$; hence the fluids appears to be mixing through molecular diffusion at $Re=1$, however for $Re = 50$ and higher, convective flow (chaotic advection) starts dominating. (Khaydarov, 2018)

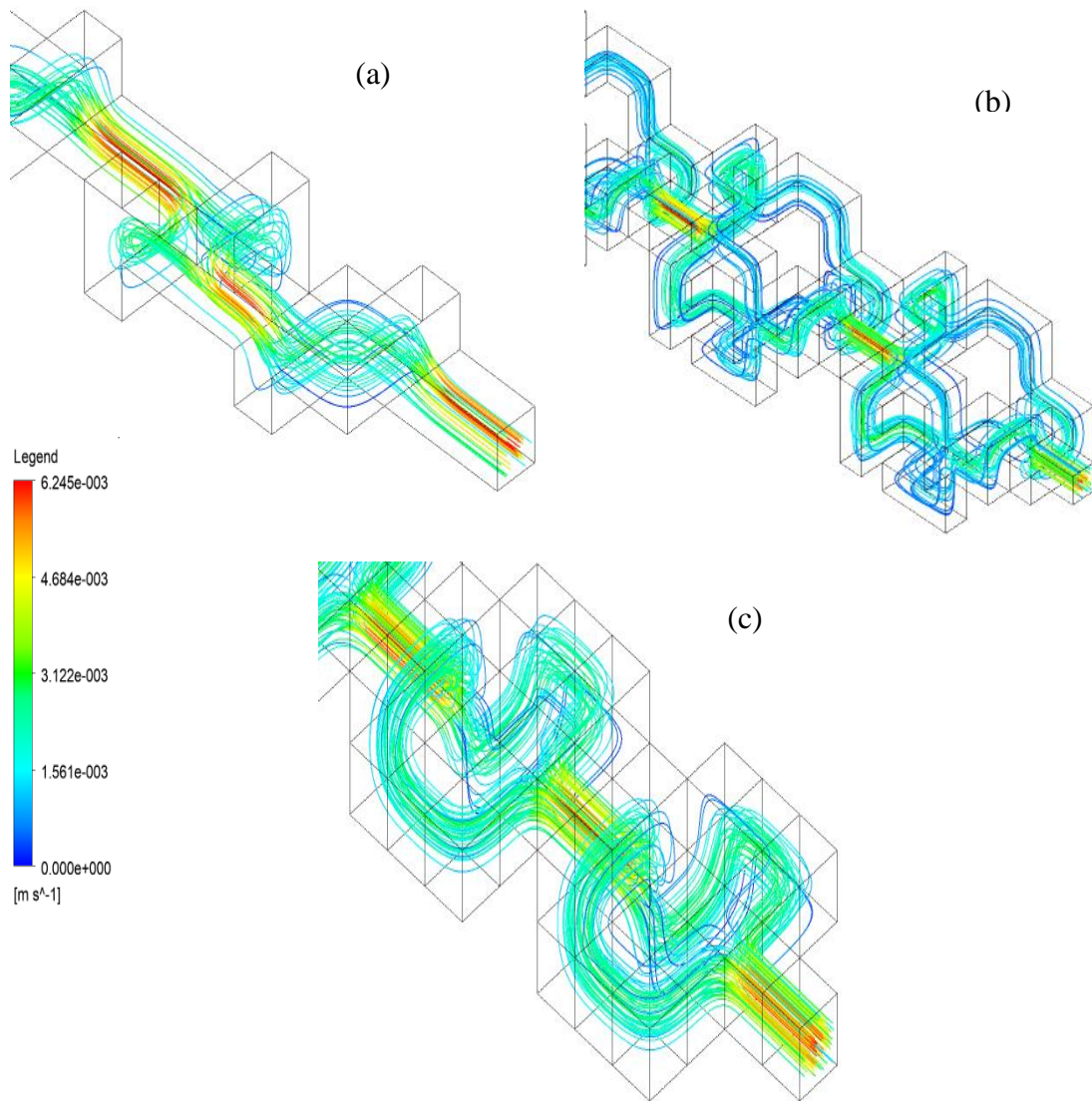


Figure 12: Stream lines at $Re=1$, for a) Chen b) Double, c) Gray SAR geometries

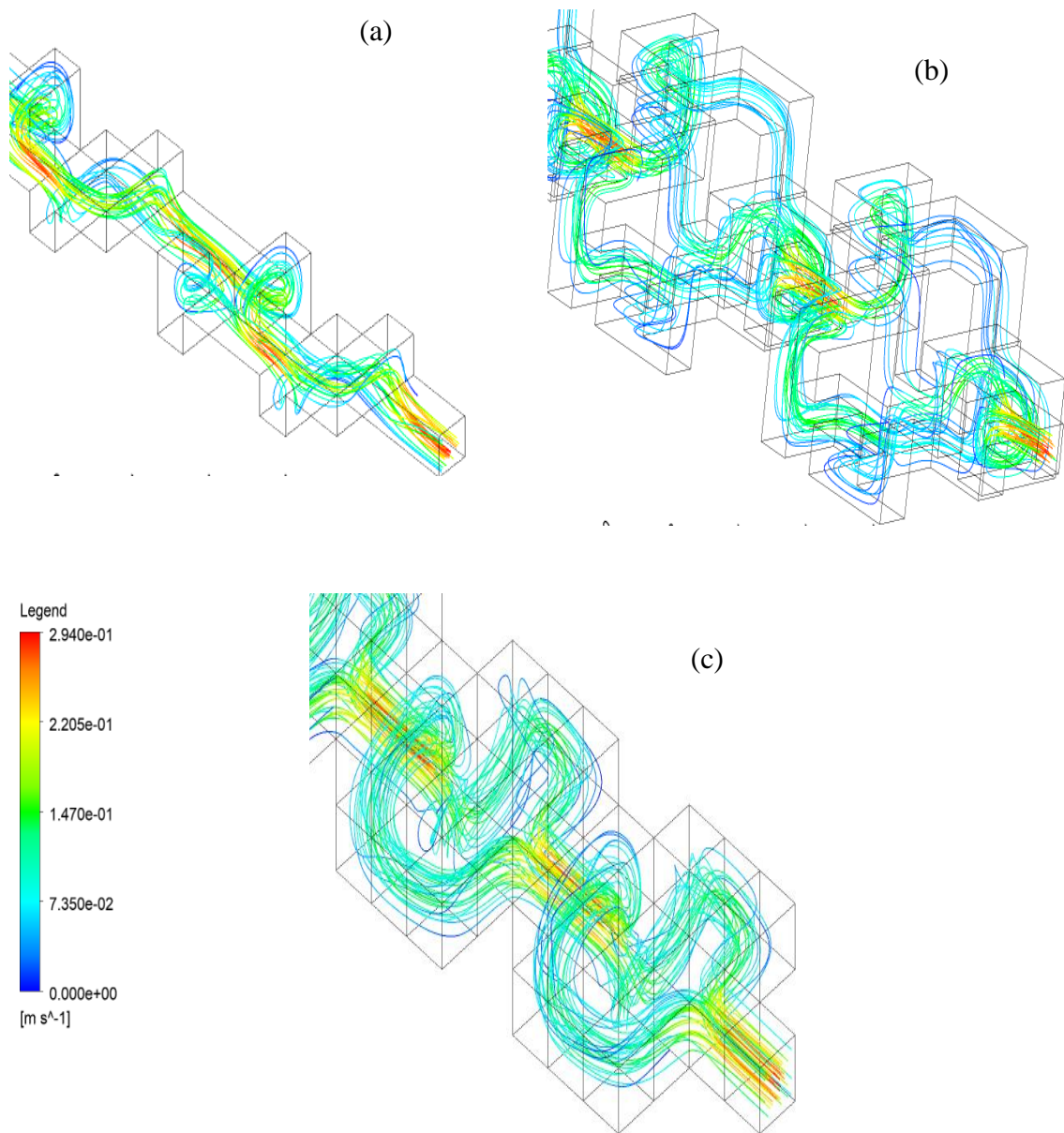


Figure 13: Stream lines at $Re=50$, for a) Chen b) Double, c) Gray SAR geometries

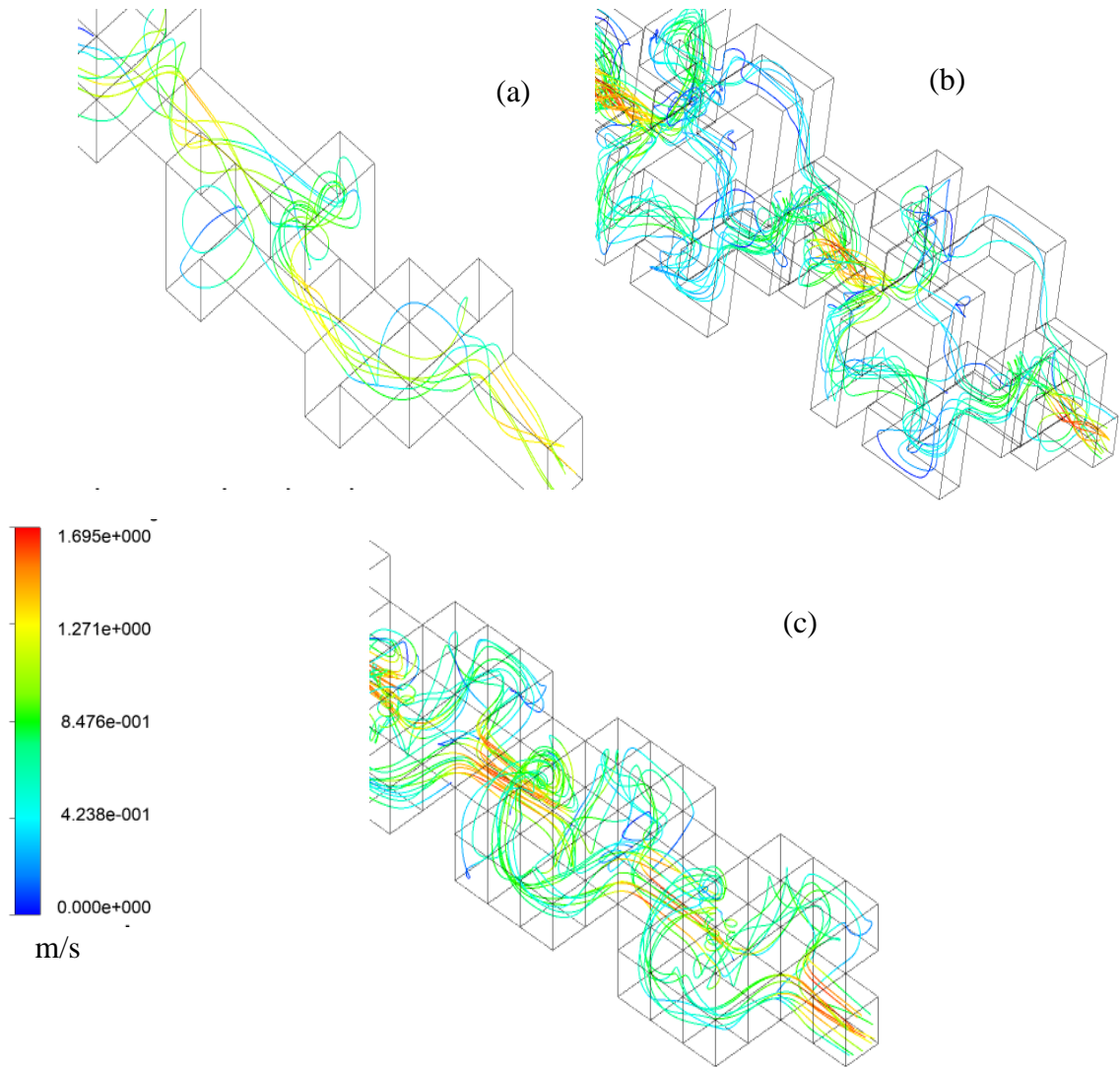


Figure 14: Streamlines at $Re=300$, for a) Chen b) Double, c) Gray SAR geometries

Figures (15-17) shows the normalized velocity vectors profiles at mid XY plane for the 3 SAR configurations for different flow conditions $Re=50$ and $Re=300$. In all the SAR configurations for $Re=50$, stagnation zones (zones with zero velocity) are observed to be located directly after 90 degree bends, which indicate the presence of recirculation zones. Also, a weak swirl in the flow can be noticed, and it becomes stronger as the Reynolds number increases to 300.

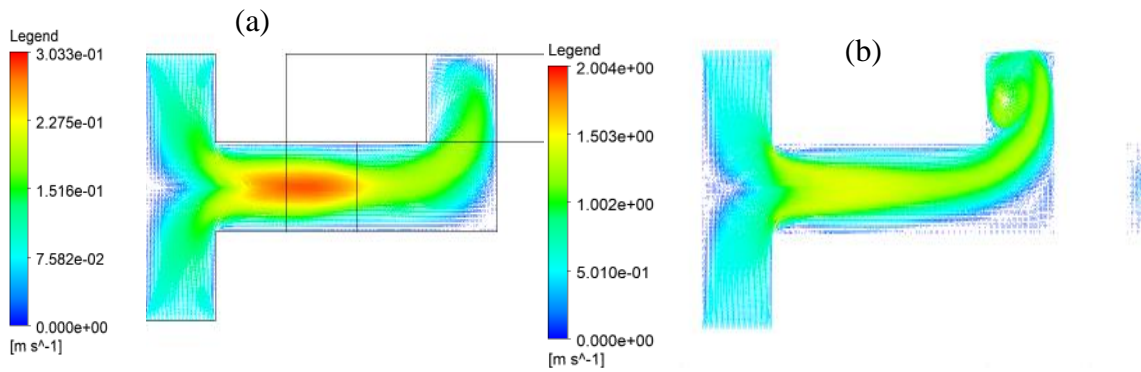


Figure 15: Velocity vectors Profiles for Chen geometry for different flow regimes, a) $Re=50$, b) $Re=300$ (at the mid XY plane $z=0.015m$)

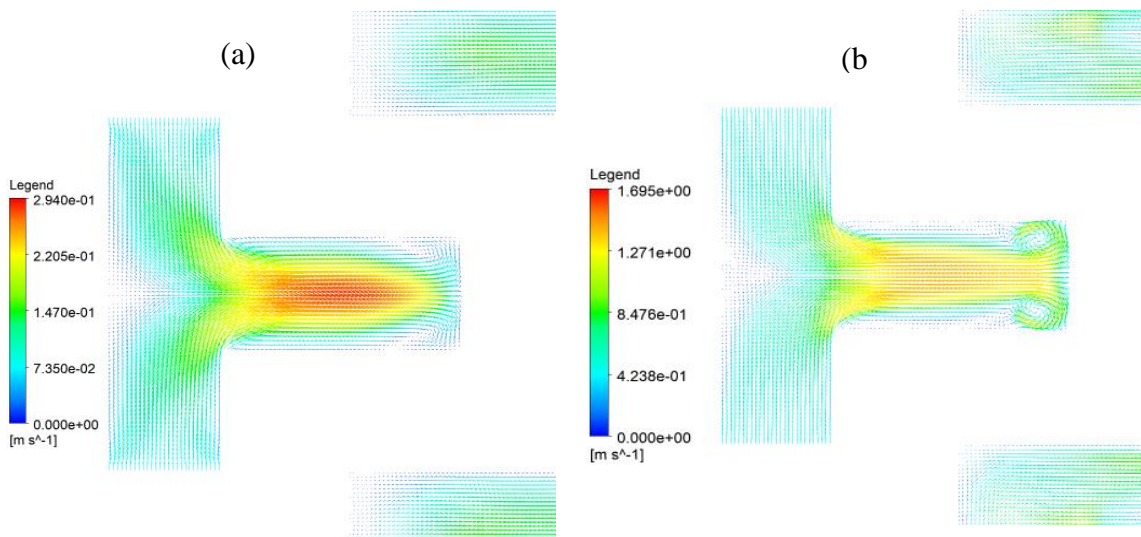


Figure 16: Velocity vectors Profiles for Double geometry for different flow regimes, a) $Re=50$, and b) $Re=300$ (at the mid XY plane $z=0.015m$)

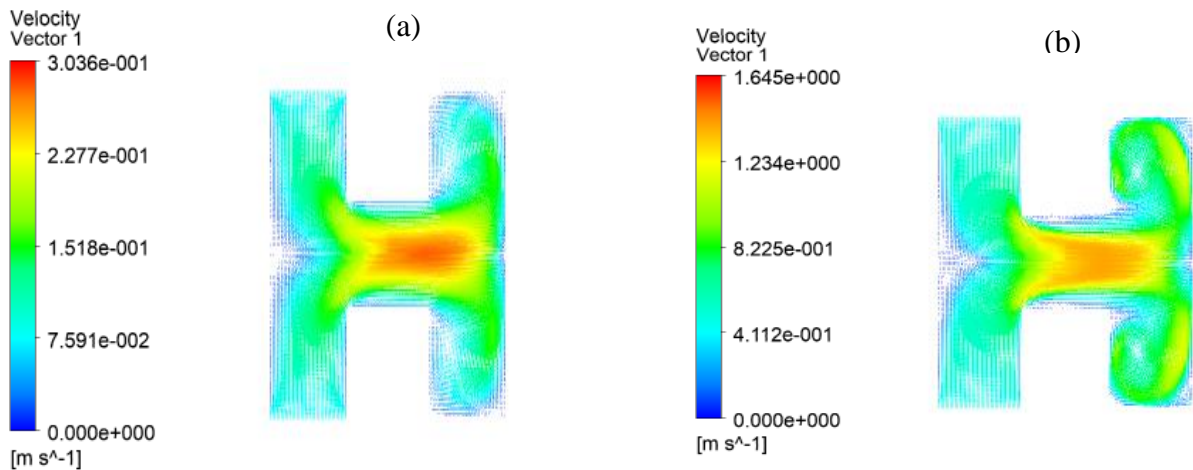


Figure 17: Velocity vectors Profiles for Gray geometry for different flow regimes, a) Re=50, and b) Re=300 (at the mid XY plane $z=0.015\text{m}$)

Mixing in a straight channel is expected to be low compared to SAR geometries as can be observed in Figures (18-20). The liquid layers in the straight channel are parallel to each other and remain in the same state as the liquid flows through the channel, even at higher Reynolds number $Re=300$ the mixing profile shows inferior mixing to any of the SAR geometries at all flow conditions.

Depending on flow conditions, mixing in the SAR configurations could be either due to fluid stratification, or due to chaotic advection arising from the continuous stretching and folding of the fluid caused by the abrupt changes in flow direction (Ghanem et al., 2013b, Khaydarov et al., 2018). The fluid layers are mostly stratified as can be clearly visualized at $Re=1$ for all the SAR geometries Figures (19 and 20); hence the chaotic advection induced by SAR mechanism is weak. At $Re=300$, the disarrangement of the fluids due to stretching, folding, and breaking of the laminar flow can be observed as well.

In addition figures 20 and 21 clearly show the progression of mixing/ destruction of the concentration gradient as the fluids proceed from the inlet to the outlet; as a result

of undergoing subsequent splitting and recombination. Mixing can be clearly seen to have improved as the number of stretching and folding mechanisms increased with higher SAR patterns.

A comparative analysis based on observation of the mass fraction contours of Figure 20, shows that at $Re=1$ the degree of mixing in Gray geometry lags behind that of the Chen and Double geometries. Mixing quality appears to improve greatly at higher Reynolds number $Re=300$ for all geometries. The next section will provide a more detailed view and numerical assessment to infer the extent of mixing improvement that each of the configurations provides

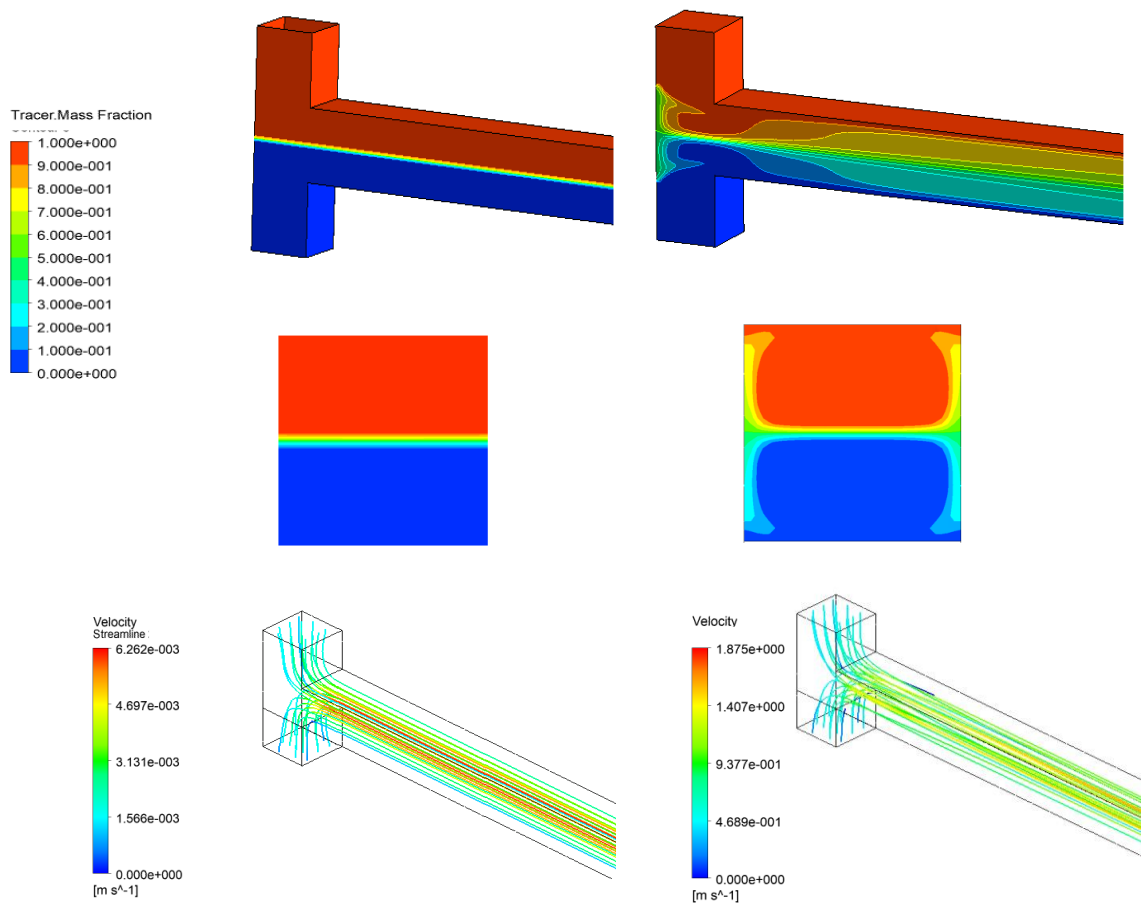


Figure 18: Isometric view, outlet scalar concentration and streamlines in the straight duct geometry (at the left column $Re=1$ and at the right column $Re=300$)

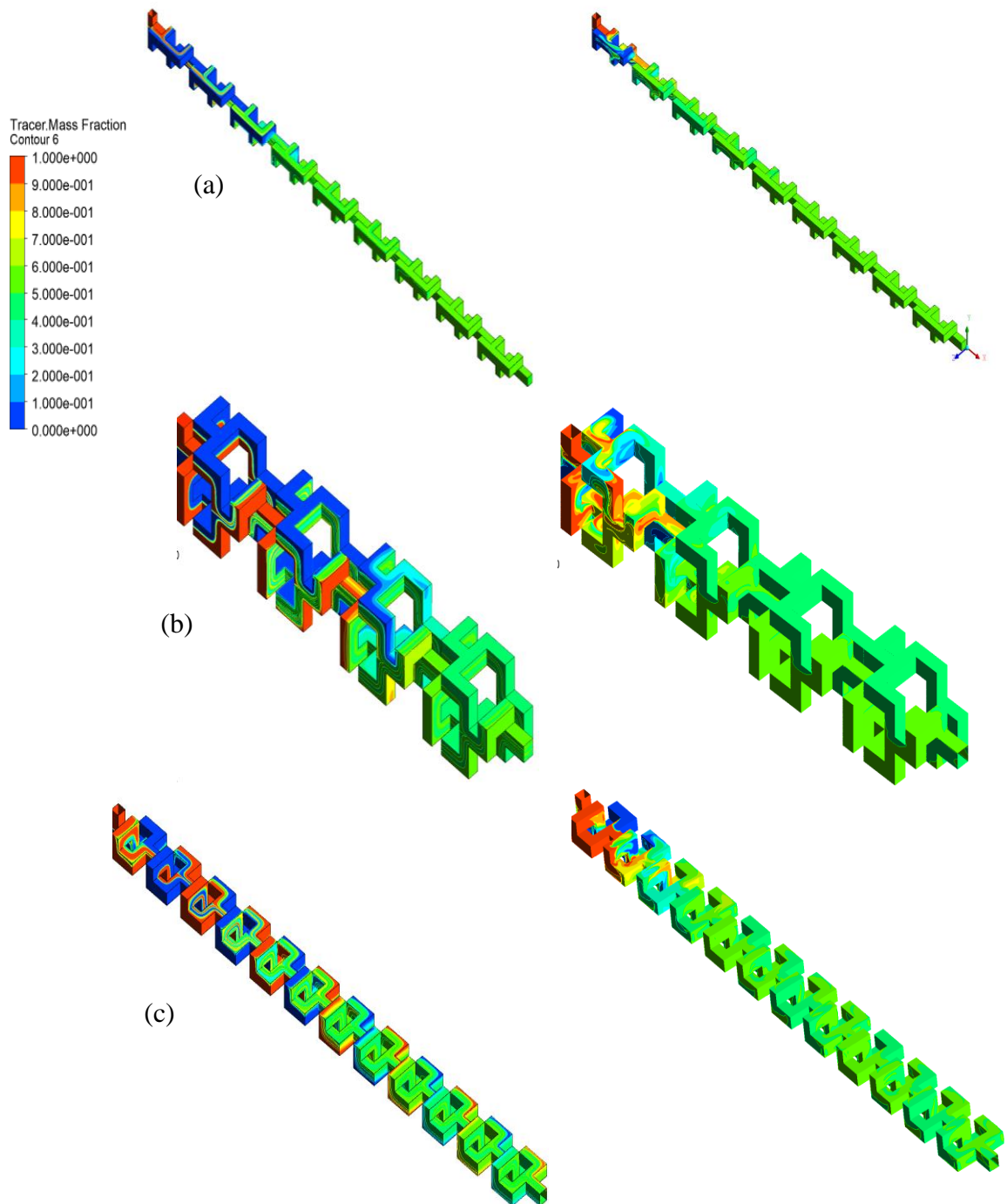


Figure 19: Isometric view, of the scalar concentrations in a) Chen, b) Double and c) Gray SAR at $Re=1$ (left column) and $Re= 300$ (right column)

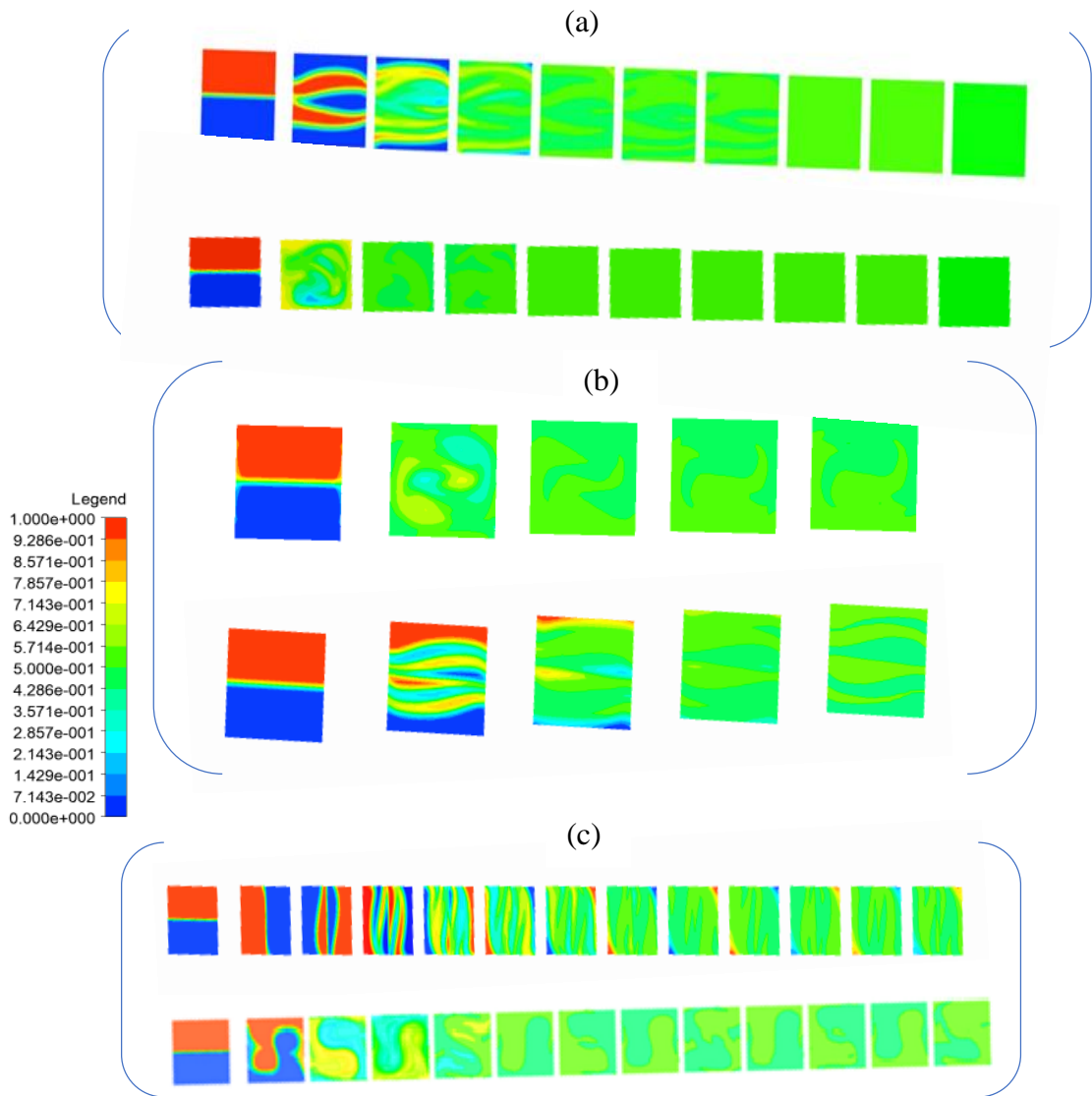


Figure 20: progression of concentration SAR geometries: a) Chen SAR, b) Double SAR, and c) Gray SAR at the upper row $Re=1$ and at the lower row $Re=300$ at the outlet of each SAR element.

2. Scalar mixing

A numerical analysis was conducted to assess the mixing behavior and establish a distinction among the different SAR configurations. Evaluating the extent of mixing

was therefore achieved by means of the mixing index I_M which was previously introduced in Chapter II.

Figure 21 shows the variation of mixing efficiency throughout the Gray geometry. The mixing index at the outlet of each element is quantified for Reynolds numbers 1 to 300 and plotted against the straight distance (x). The results show that for $Re < 200$ even after exhausting all its 12 elements ($x=0.186\text{m}$) the mixing index fluctuates between being 88% at $Re=1$, 69% at $Re=10$, 94% at $Re=50$, and 80% at $Re=100$. Nonetheless the mixing peaks at 99% when $Re = 200$ or 300 attained after a distance $x = 0.111\text{ m}$ and $x=0.126\text{ m}$ corresponding to 8 and 9 elements of Gray geometry respectively.

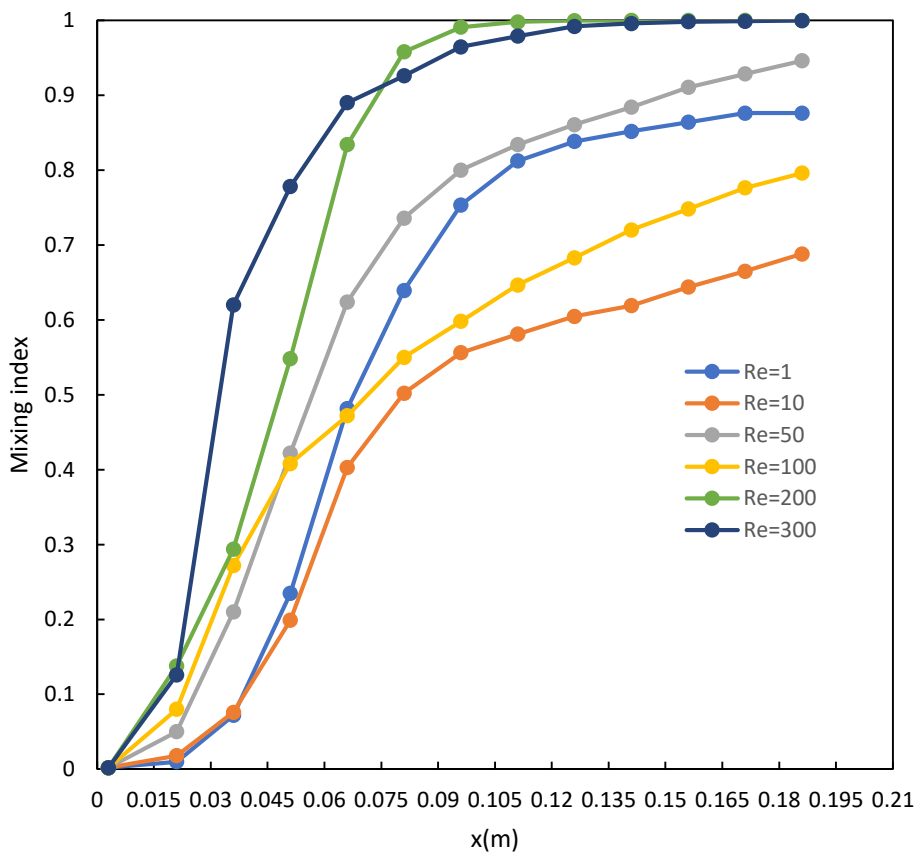


Figure 21: Mixing index along the length of Gray geometry evaluated at the exit of every SAR element.

Figure 22 compares the overall mixing efficiency of the Gray SAR, by assessing its mixing index at the outlet of the full geometry as a function of the flow conditions. The mixing index which was initially 88% at $Re=1$ drops by 19 % as Re increases to 10. However, as the flow conditions are changed to $Re=50$ the mixing index increases again to reach a value of 94% to decrease again by 15 % at $Re=100$. The mixing index increases again to reach a maximum of 99.9% at $Re=200$ and 300.

The drop in mixing efficiency as Reynolds number increase from 1 to 10 can be explained by the fact that in these particular flow conditions mixing takes place primarily through diffusion (akin to stratified flow regime). Although SAR patters introduce chaotic advection; it is still weak compared to diffusion effect. The introduction of secondary flows and the deviation from SAR principle shortens residence time. Since the mixing quality is dependent on the mixing time, increasing Re from 1 to 10, would shorten the residence time for the fluid particles to diffuse and thus deteriorates the mixing quality. (Khaydarov et al., 2018, Hermann et al., 2018)

When $Re \geq 50$, chaotic advection becomes more prominent, and secondary dean flow is introduced which causes swirling effect as observed in Figure 18a. The swirling effect increases the interfacial area exponentially, lengthening the fluid path, hence the convective influence on mixing compensates for the reduced residence time due to higher velocity at higher Reynolds numbers. However for $Re=100$, the flow rate becomes high enough to significantly decrease the residence time of the fluid stream which consequently decrease the efficiency of the mixing process. (Khaydarov. et al, 2018)

Nonetheless, beyond Re 200, the effects of Dean of secondary flow intensifies, engulfment flow starts taking effect, which promotes asymmetrical swirling (seen in figure 23) and hence lengthen the fluid path and promotes mixing. (Nguyen, 2012).

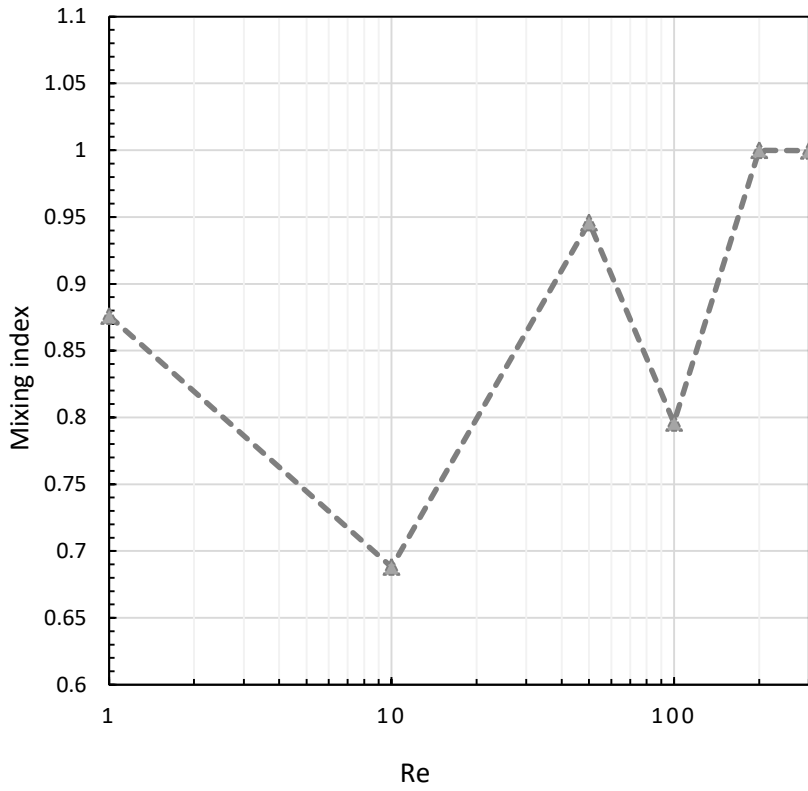


Figure 22: Mixing index at the outlet of Gray SAR as a function of various flow conditions.

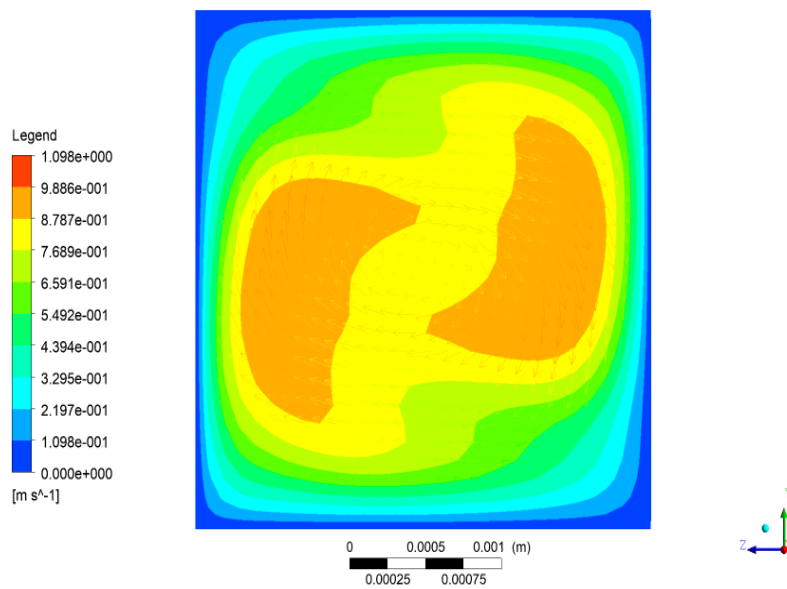


Figure 23: Velocity profile of Double SAR at Re=200

Figure 24 shows the variation of mixing efficiency throughout the Double SAR geometry (Figure 11c). The mixing index at the outlet of each element is quantified for Reynolds numbers 1 to 300 and plotted against the straight distance (x). The results show that for flow conditions $Re=200$ and $Re=300$, 3 elements (at $x=0.087m$) are enough to reach almost complete homogeneity (a mixing index $>99\%$). However, for lower Reynolds numbers reaching the maximal mixing efficiency of the double geometry requires all its 4 SAR elements (at $x=0.114m$), which amounted to a mixing index equivalent to 97%, 96%, 94%, and 97.6% for $Re=1$, $Re=10$, $Re=50$, and $Re=100$ respectively.

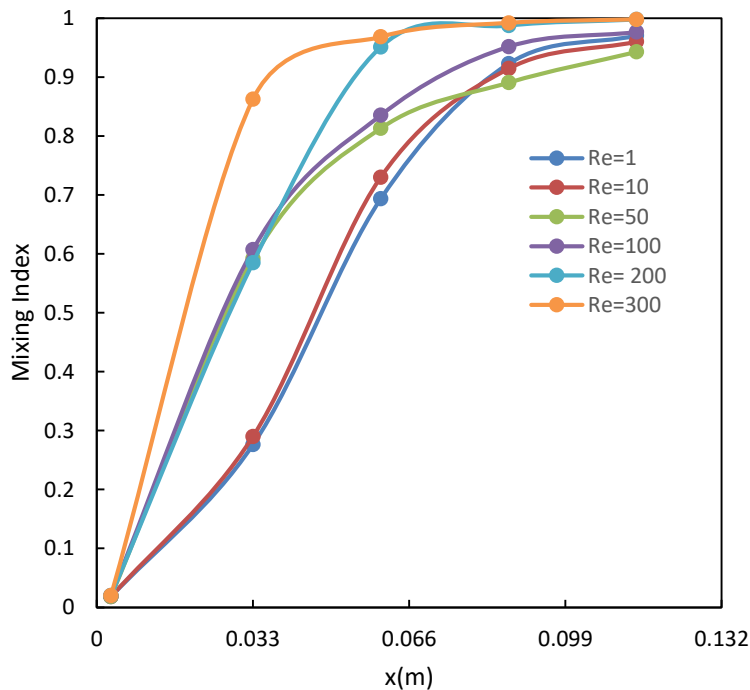


Figure 24: mixing index along the length of Double geometry evaluated at the exit of every SAR element

Figure 25 compares the overall mixing efficiency of the Double by assessing its mixing index at the outlet of the full geometry as a function of the flow conditions. For

all Reynolds number studied, the mixing index is $>94\%$; hence, the effect of the Reynolds number is minimal. The mixing index is 97% for $Re=1$; it decreases by 1% when $Re=10$ and further decreases by 2 % when $Re=50$. At $Re=100$, the mixing index increases to 98% and further to 99% at $Re=200, 300$.

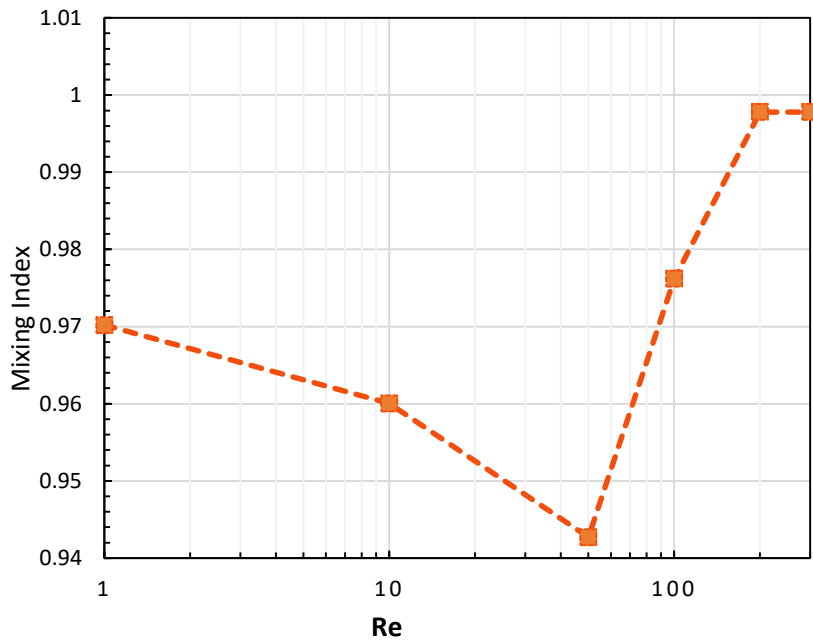


Figure 25: Mixing index at the outlet of Double SAR as a function of various flow conditions

Similar to the argument presented for the behavior of Gray SAR geometry, in the Double SAR geometry as Reynolds number and hence flow rate increase from 1 to 10 the slight decrease is due to the decrease in residence time. At $Re=50$, the chaotic advection becomes more prominent, but it is still weak for the swirling effects to compensate for the decrease in residence time; hence the decrease by 2 % when Reynolds number increases from 10 to 50. At $Re= 100$, the chaotic advection becomes more dominant, which causes a further increase in mixing efficiency. At $Re= 200$ and 300 , Dean flows

intensify, which, as mentioned before, lengthens the fluid path and promotes mixing. (Nguyen, 2012, Khaydarov et al. 2018).

However, the variation in the mixing indices is minimal, which indicates that the effect of the flow conditions on the mixing efficiency is very minimal.

Figure 26 shows the variation of mixing efficiency throughout the Chen SAR geometry (Figure 11a). The mixing index at the outlet of each element is quantified for Reynolds numbers 1 to 300 and plotted against the straight distance (x). The results shows almost perfect mixing ($IM = 0.997$) is reached for $Re=300$ and $Re = 200$ only after 4 SAR elements (straight length $x=0.114m$). Whereas for lower Reynolds numbers, reaching the same level of homogenous mixing necessitated 6-7 SAR elements (at $x= 0.168, 0.195m$).

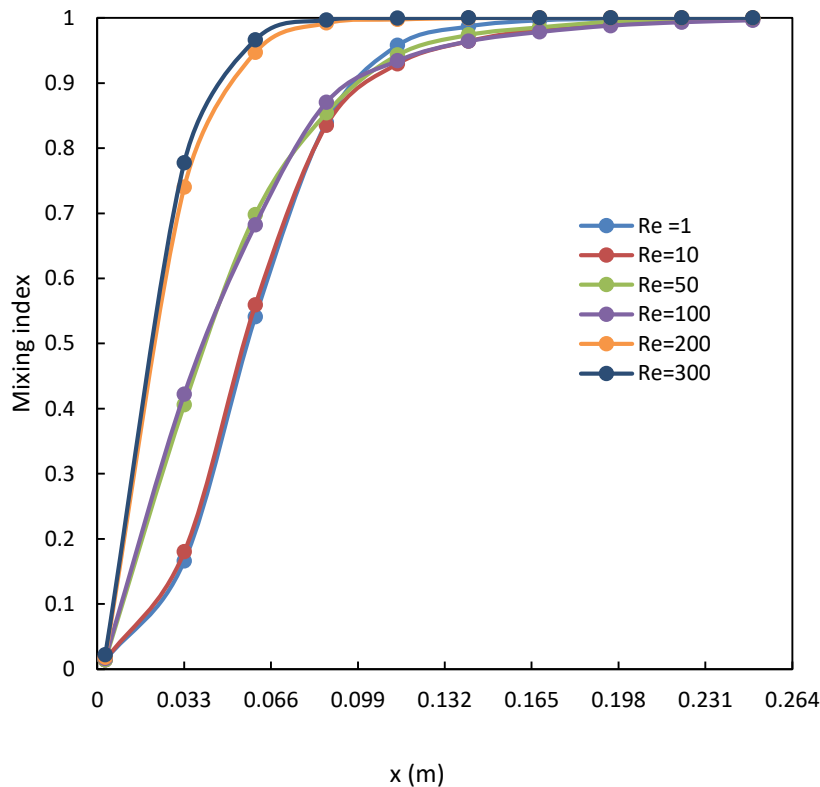


Figure 26: Mixing index along the length of Chen geometry evaluated at the exit of every SAR element

Figure 27 compares the overall mixing efficiency of the Chen SAR by assessing its mixing index at the outlet of the full geometry as a function of the flow conditions. The results show that the mixing index is always $> 99\%$. There are slight fluctuations consistent with what was seen in Gray and Double SAR geometries. For instance, there was a slight decrease in the mixing index when Reynolds number increased from 1 to 10, followed by a slight increase then decrease in the mixing index as Reynolds number progresses from $Re=10$ to $Re=50$ to $Re=100$. Then the mixing index reached a maximum for $Re=200$ and $Re=300$. These observations align with the behavior of the flow in flow regimes explained earlier. However, the variations in mixing efficiency are almost negligible. Hence, it can be assumed that the effects of the flow conditions on the mixing efficiency of the Dray SAR are minimal.

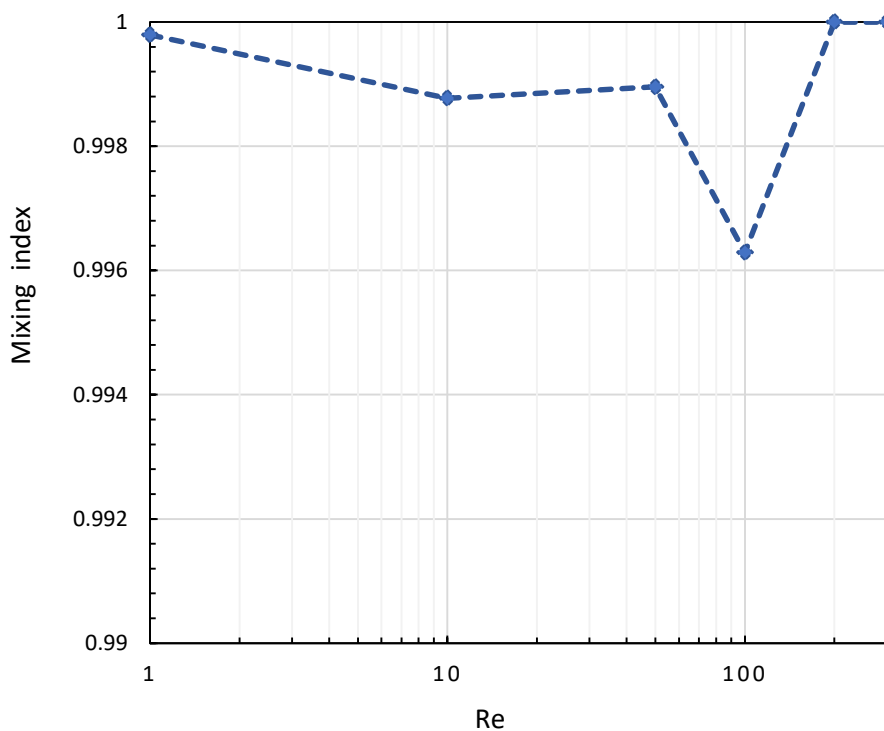


Figure 27: Mixing index at the outlet of Chen SAR as a function of various flow conditions

Figure 28 compares the overall mixing efficiency of all the configurations under study by assessing the mixing index at the outlet of each geometry as a function of the flow conditions. It is clear from the results that the mixing efficiency is minimal in the straight duct geometry compared to the SAR geometries, not amounting to more than 10% of mixing.

For all flow conditions, the Chen SAR recorded an optimal efficiency > 99%, and the Double SAR recorded optimal efficiency > 94%. Whereas, the Gray SAR witnesses fluctuations in its mixing efficiency as it dropped by 19 % (from an initial value of 88% at Re=1) as Re increased from 1 to 10. Then it increased again to reach a value of 94% at Re=50, to decrease again by 15 % at Re=100. The mixing index increases again to reach an optimal value >99% at Re=200 and 300.

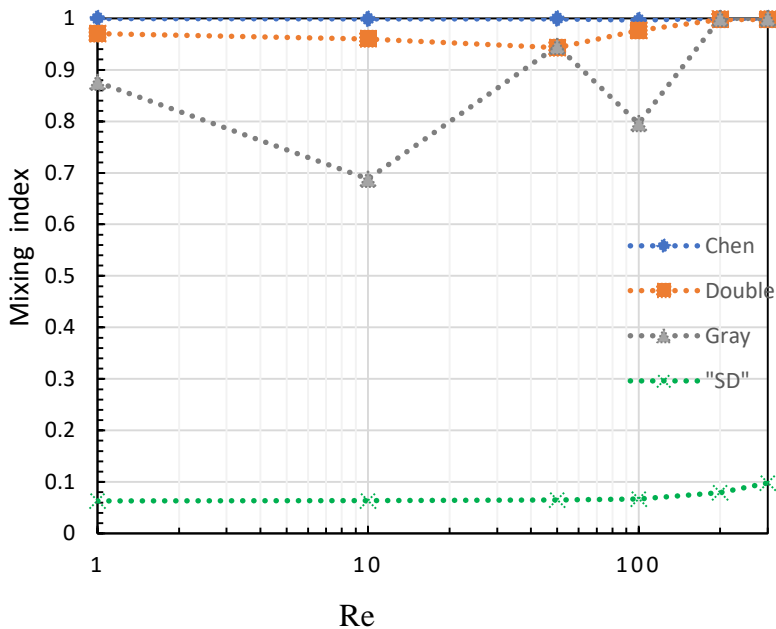


Figure 28: Mixing index vs. Re for all three SAR configurations combined and the straight duct.

Hence, the effect of the Reynolds number is minimal for Chen and Double SAR geometries but it more prominent for Gray's. This result can be attributed to the geometric construction of the former 2 SAR geometries. The fluid in Chen SAR undergoes more splitting and recombination (+50%) compared to Gray SAR. While, the Double SAR undergoes successive splitting and recombination, which creates multi-laminations and allow faster homogenization of the concentration profile. These characteristics help reach high mixing efficiency independent of the flow conditions.

In addition, it can be observed that for $Re < 200$ (chaotic advection flow regime), the Chen SAR records the highest mixing efficiency followed by the Double and then the Gray SAR geometries. However the difference in mixing performance between Chen and Double SAR is small enough to consider them comparable in that field.

On the other hand, when $Re = 200$ and $Re = 300$, all the SAR geometries recorded mixing efficiency $> 99\%$, due to the introduction of dean vortices and asymmetrical swirling which lengthen the fluid path and leads to optimal mixing.

To understand more about the behavior of the fluid within the SAR geometries, the mixing index is assessed relative to different SAR lengths presented in chapter IV.

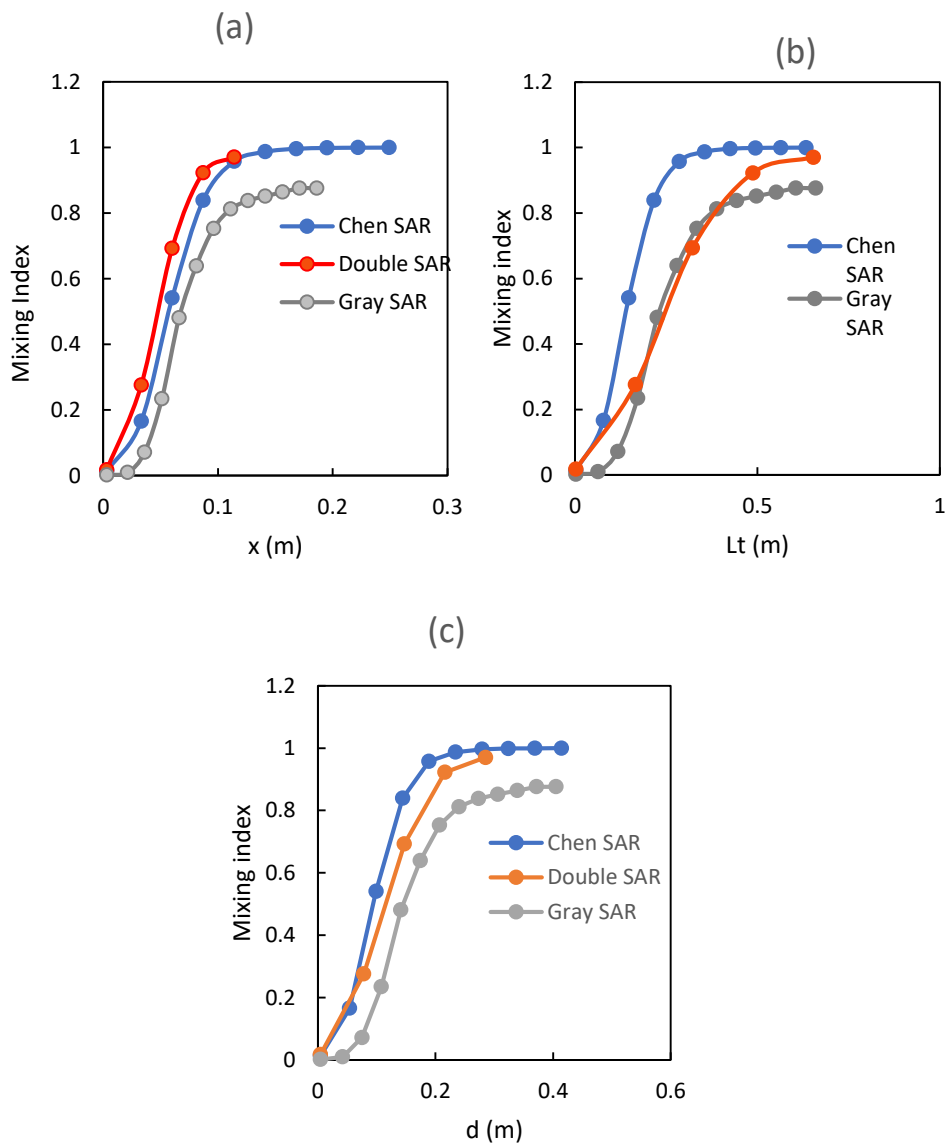


Figure 29: Evolution of the mixing index along different lengths of the SAR configurations at $Re=1$

The above figure represents mixing index as a function of different lengths of SAR geometries at $Re=1$. According to Figure 29a which plots the mixing index as a function of the straight distance at $Re=1$, the mixing indices for all SAR geometries increase along their lengths. The Double SAR was found to reach its maximal efficiency 97% faster than the other 2 geometries which is due to its compact geometry. However

according to figures(29b and 29c) , which plot the mixing index as a function of the total length (L_t) and the developed length (d), the Double SAR would require longer distance to reach the same efficiency. Hence both Chen and Double SAR require similar equivalent lengths ($L_t = 0.65\text{m}$ and $d=0.114\text{m}$) to reach their optimal efficiencies which are 99% and 97 % respectively. Whereas, the Gray SAR lags behind in terms of its efficiency only reaching a maximum of 88%. (Appendix B has mixing index as a function of different lengths of SAR geometries for all the flow conditions under study)

It can be concluded that Chen and Double geometries have demonstrated a superior mixing performance to that of the Gray geometry for all the flow conditions, except when $Re=200$ and $Re=300$, as the difference in mixing efficiency becomes negligible. Although the Double geometry displays a comparable mixing efficiency to the Chen SAR geometry, it still lags behind it. These increased efficiencies in Chen and double geometry compared to Gray geometry, particularly in chaotic advection conditions, are due to their geometric construction, allowing better lamination and more contact between fluid layers, facilitating diffusion. The effect of lamination-based mixing diminishes as swirling effects becomes more prominent.

B. Pressure drop and friction factor

Mixing performance alone cannot be considered the sole determinant of SAR geometries efficiency. A trade-off between performance and energy costs is necessary when considering implementing a design in any industrial application. Hence, pressure drop, which is an essential factor that dictates the power requirement of a system, is calculated for all the geometries under all the flow conditions in this study.

As mentioned in the previous sections, the pressure drop is measured between the outlet and the mixing plane where the 2 inlets meet. To evaluate the accuracy of the computational results. The computational pressure drop values across the straight duct are compared to the theoretical pressure drop calculated from equations 6 and 7 in Figure 30. This figure shows that the computational values for pressure drop clearly agree with the theoretical values.

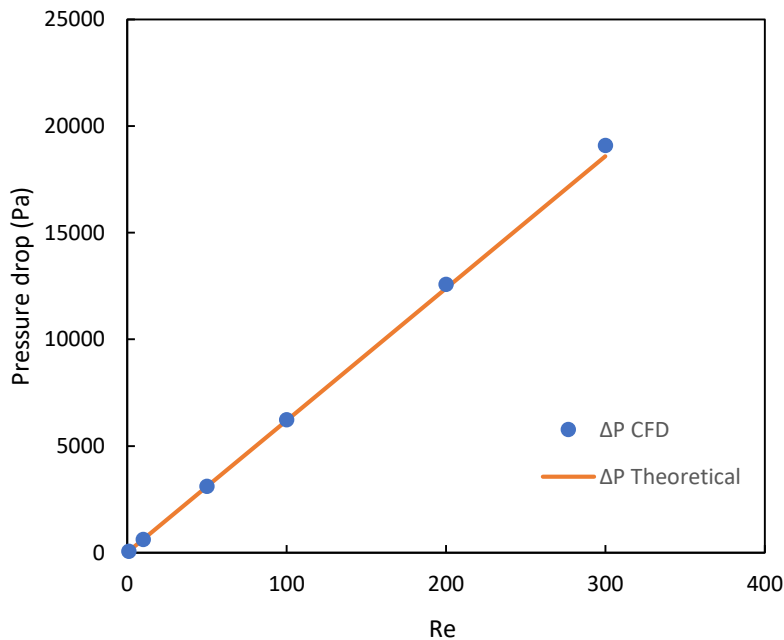


Figure 30: Validation of the Pressure drop

Figure 31 represents the pressure drop across each geometry. As expected, the pressure drop is directly proportional to the Reynolds number in the straight duct. This characteristic is evident in all the other SAR geometries as well. Furthermore, it can be noted that Chen and Gray geometries have lower pressure drop compared to the straight duct for Reynolds number lower than 200. Nonetheless, in the Double geometry, the

pressure drop is consistently low compared to all other geometries for all flow conditions under study.

This behavior can be attributed to the fact that the velocity of the straight duct, where the flow streams are always parallel, is higher compared to the SAR geometries. The reason is that splitting the flow stream in SAR geometries will half the velocity of the incoming flow, which means that the average Reynolds number will be smaller than that of the straight duct. Double geometry has an additional advantage due to the double split of the flow streams, which further attenuates the velocity, and hence its average Reynolds number will be even lower than Chen and Gray geometry. 70 % of the volume of Chen geometry has a velocity equivalent to half the inlet velocity, 77% for Gray geometry, and 50 % for the double geometry. The double geometry has a further 37% of its volume, where the velocity is equivalent to a quarter of the inlet velocity.

As mentioned in the earlier section, secondary Dean Vortices become more dominant at $Re=200$ and beyond. Hence due to the more vigorous traverse motion and higher wall friction that are dominant at these flow conditions, the previous SAR effects on lowering the pressure drop are heavily attenuated. The presence of 90-degree bends significantly increases the pressure losses.

Even though the SAR mechanism's effect of decreasing head loss is attenuated, the Double geometry still provides an improvement in hydrodynamic performance over the straight duct and the other 2 SAR geometries due to its unique design, which maximizes the effect of the SAR mechanism.

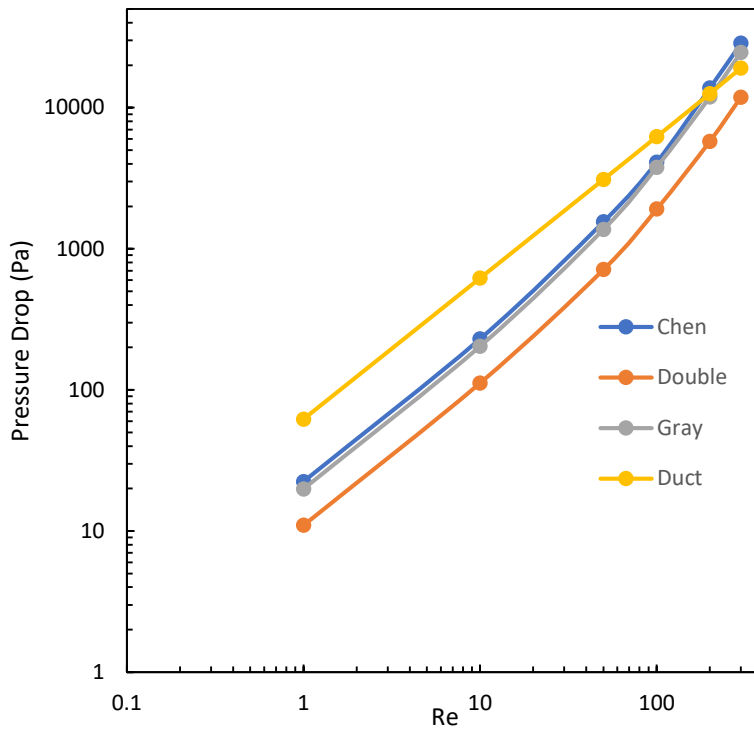


Figure 31: Pressure drop across the 3 SAR geometries

Pressure drop can translate directly into energy consumption by means of energy per unit volume of treated fluid, defined as:

$$E_V = \frac{Q \times \Delta P}{V} \quad (27)$$

Where Q is the volumetric flow rate in m^3/s

ΔP is the pressure drop in Pa

and V is the volume of the geometry in m^3

Energy consumption is plotted for the geometries under study against the flow conditions (figure 32), and against the mixing efficiency/mixing indices obtained at the outlet of the geometries (figure 33)

The trends observed in energy consumption (Figure 32) are similar to what is observed for the pressure drop since they are directly proportional. Hence the arguments used above to explain the pressure drop for the different flow conditions across the different geometries under study also applies to the energy dissipation. Geometries with the least pressure drop have the lowest energy dissipation and hence the most energy efficient and it was the Double geometry in this study.

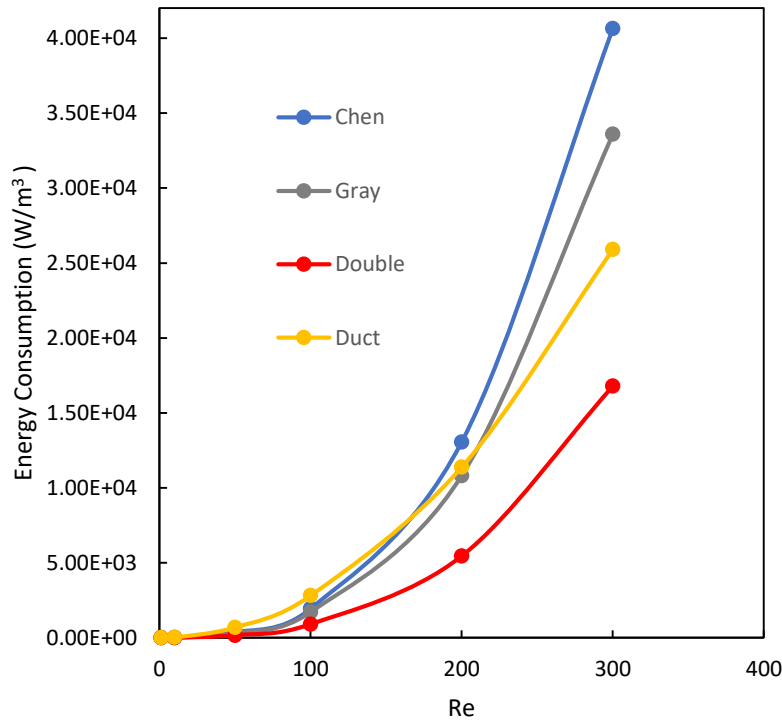


Figure 32: Energy Consumption as a function of flow conditions in the 4 geometries under study

Figure 33 shows that the Double and Chen SAR geometries are the most energy efficient, attaining comparable efficiencies >95% for lower energy consumption compared to Gray SAR. When the energy consumption is greater than 10000 W/m³ associated with increased Dean secondary flows i.e. Re= 200, and 300 (Figure 32) all the

SAR geometries has already attained optimal mixing efficiencies >99 %. This observation, shows that the SAR mechanism effect deteriorates at higher flow rates; as the geometries witness a surge in the energy consumption and costs with little to no effect on the mixing efficiency.

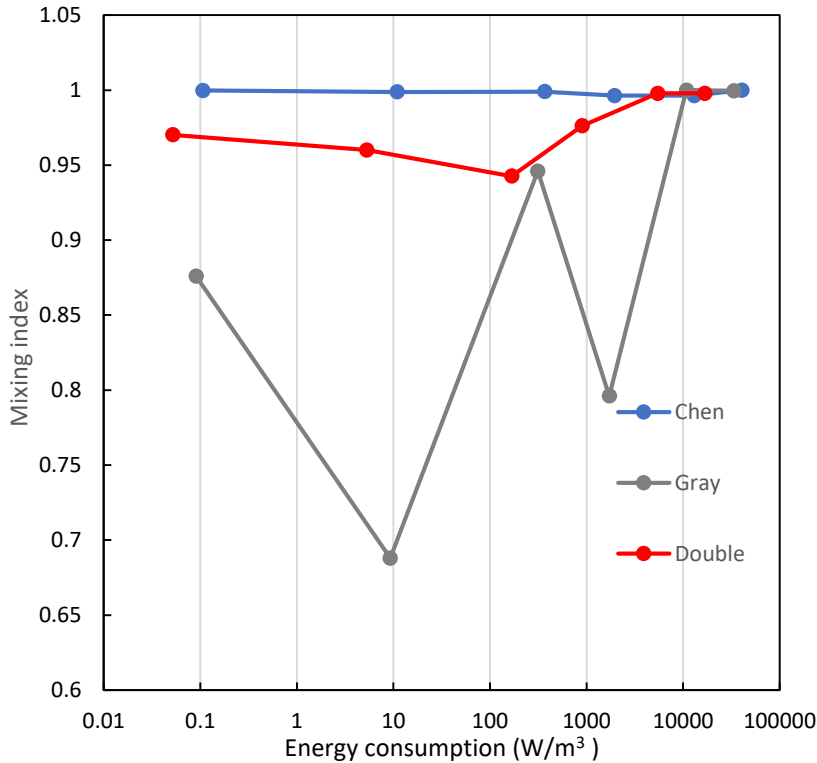


Figure 33: Mixing Index as a function of energy consumption

The hydrodynamic performance of all geometries can be further evaluated using friction coefficient f as discussed in chapter III (calculated using equations 9 and 10).

Figure 34 shows the normalized friction coefficients, where f_0 (calculated by Eq 9) represents the friction coefficient in the straight channel, which exhibits the lowest friction losses because it has the lowest number of bends. For higher Reynolds numbers (higher flow rates), higher friction factors are obtained in all SAR geometries; double geometry exhibits the highest friction, which reached 5 times that in a straight duct at

Reynolds number 300. This behavior is consistent throughout all flow conditions. Despite having the least pressure drop, the double geometry possesses the highest friction coefficient is an expected result due to its double split and recombination design and is further evident in equation 10.

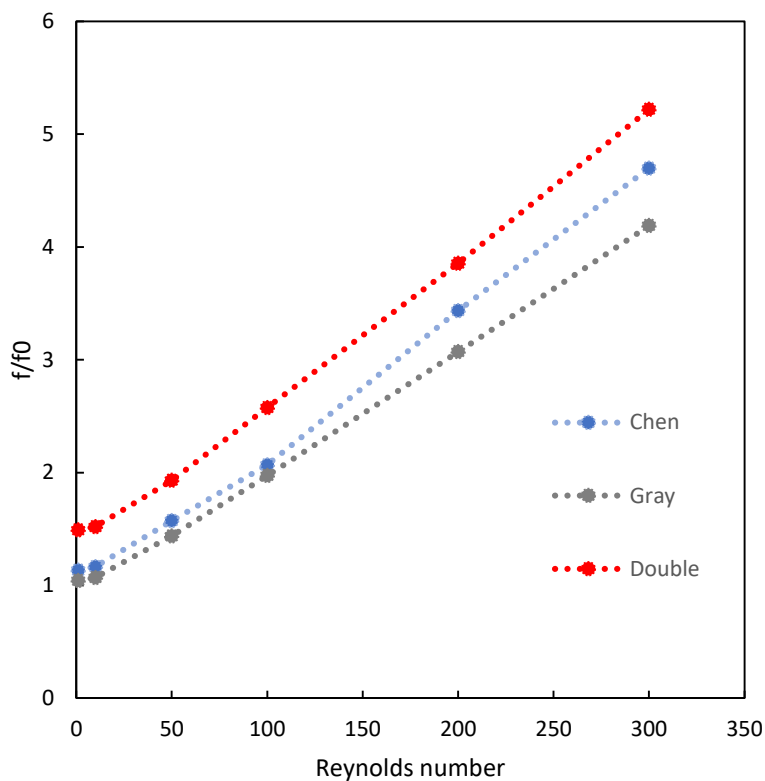


Figure 34: Normalized friction factors

C. Thermal and Hydronamics Analysis

This section presents the results of the heat transfer studies. The computational fluid dynamics simulations were carried out for the same fluid flow of water-ethylene glycol mixture (98 wt% ethylene glycol) in the 3 different SAR configurations as well as in the straight channel. The simulations are generated for Reynolds numbers 1, 10, 50,

100, 200 and 300. The following sections will therefore elucidate the differences in heat transfer among these 4 configurations for different flow conditions.

1. Nature of heat transfer

The first step in heat transfer analysis is studying the regime through which the heat transfer phenomenon occurs. It could take place as natural, forced or mixed convection. Natural or free convection relies on buoyancy forces to induce fluid motion. In contrast, forced convection occurs due to the velocity of the imposed flow. On the other hand, mixed convection occurs when both natural and forced convection are equally present (Sigh A. et al, 2015)

The nature of heat transfer can be identified through dimensionless numbers such as the Grashof number, and Richardson number. (Shah et al., 2017). They can quantitatively determine whether the natural convection is dominant over the forced convection or vice versa. (Rashidi et al., 2014)

Natural convection is dominant when Richardson is too large, it becomes insignificant when it is close to zero. The effect of both natural and forced convection coexist and become equally effective when Ri have finite values (Sigh A. et al, 2015)

The table below shows the values of Richardson number relative to the different flow conditions investigated in this work.

Table 6: Richardson number

Re	1	10	50	100	200	300
Ri	93.00	0.93	0.037	0.0093	0.0023	0.001

It can be deduced from Table 6 that for $Re = 1$ the heat transfer is due to free convection, for $Re=10$ it is due to combined free and forced convection. Whereas for $Re = 50,100, 200,$ and $300,$ it occurs as a result of forced convection.

2. Model Validation for the Thermal Analysis

To verify the accuracy of the heat transfer numerical solutions, computations of the thermally developing flow forced convection are carried out in the straight duct. The computational results obtained through the simulations are then compared to the theoretical values obtained from the following equations:

$$\overline{Nu} = 3.66 + \frac{0.0668Gz}{1 + 0.04Gz^{2/3}} \quad (28)$$

Where G_z is the Graetz number defined as (29)

$$Gz = \frac{D}{L} \times Re \times Pr$$

And Re is the Reynolds number,

Pr is Prandtl number. (Bejan; & Kraus, 2003)

Figure 35 presents the comparison between the computational values obtained in the current work for various Re values, and the theoretical value of Nu number for the straight duct. A maximum relative error of 8% was calculated between the theoretical and computed values of the Nusselt number. Hence the results are deemed acceptable to continue the simulations on SAR geometries.

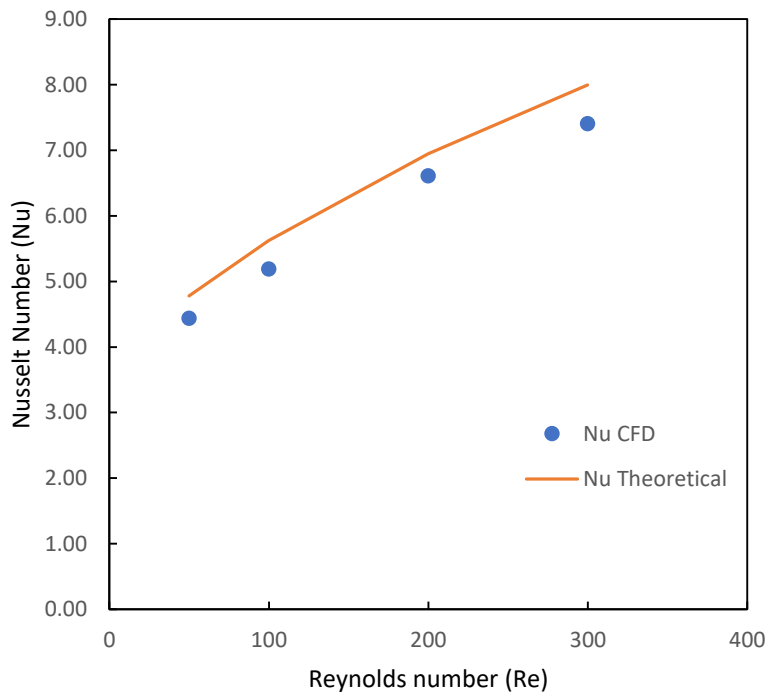


Figure 35: Validation for Nusselt number in straight channel

3. Convective heat transfer

The passive effect of the SAR configurations on hydrodynamics is translated in the subsequent thermal behavior of the flow. Figures 36 represents the Double SAR geometry and shows how the changes in velocity profiles manifests themselves in the thermal components of the flow.

The SAR geometry has isothermal walls set at 350 K, while the flow is initially at 300K. Almost negligible heat transfer is observed in low velocity areas adjacent to the SAR bends and near the walls, as poor heat evacuation causes overheated localized fluid zones. However, low temperature zones around the convex corners are linked with the higher flow velocities in these regions after the breakage of the hydrodynamic boundary layer accompanied by a sudden increase in the local heat-transfer rate in regions close to the bend. In addition between two subsequent elements a hot strip in the flow core exists

in the middle between two zones of lower temperature which is a sign of SAR mechanism. That is due to the continuous stretching and folding of the laminations which causes the fluid that was near the wall to relocate in the middle after the converging zone of SAR. As the fluid progresses through the SAR mixer its temperature homogenizes and hence heat transfer is increased. (Ghanem et al, 2013b)

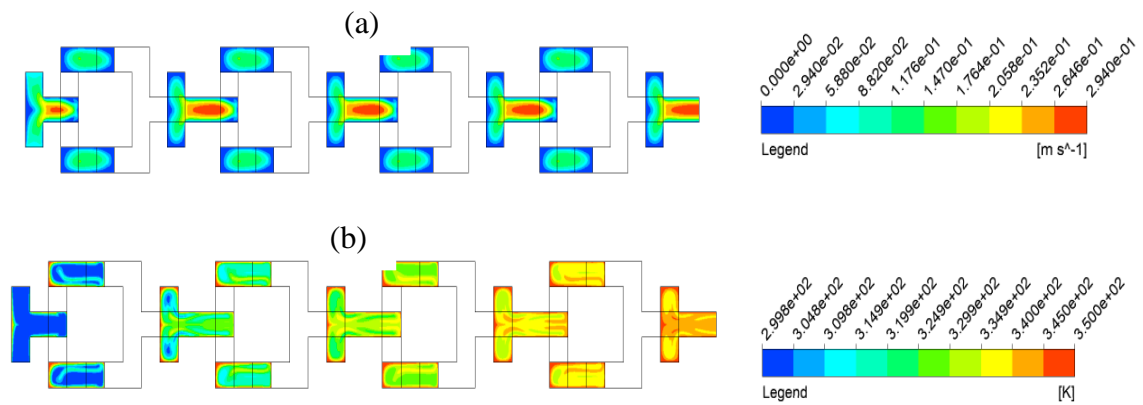


Figure 36: Contours of velocity (a) and temperature (b) in Double geometry at Re=50

4. Numerical Analysis of heat transfer

Nusselt number was calculated according to equation (17). It is used to better quantify the effect of heat transfer within the SAR geometries. Figure 37 shows the average Nusselt number at the outlet of each SAR element. Figure 38 shows the average Nusselt number as a function of the straight distance in the straight duct.

The results show a clear improvement of heat transfer with increased flow rate as exemplified by the proportional relation between Nusselt number and Reynolds number. In addition; it is noticed that the average Nusselt number deteriorates as the flow progresses in the straight duct, while it remains constant in all SAR geometries, a behavior

pertinent to bakers' transformation pattern seen as well in the work of (Creysseles et al, 2015).

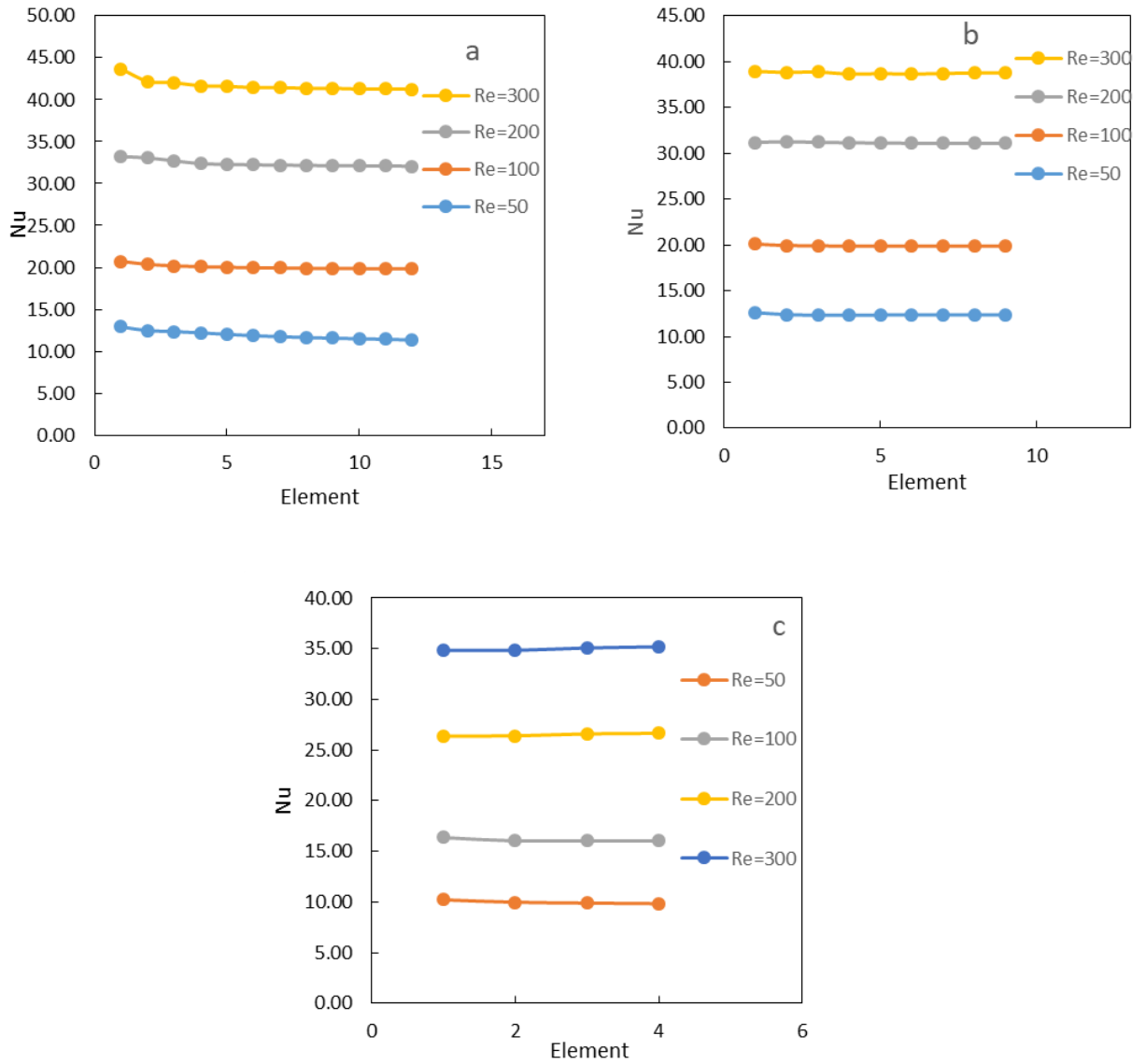


Figure 37: Average Nusselt number per SAR element as a function of a) Gray, b) Chen, and c) Double SAR geometries.

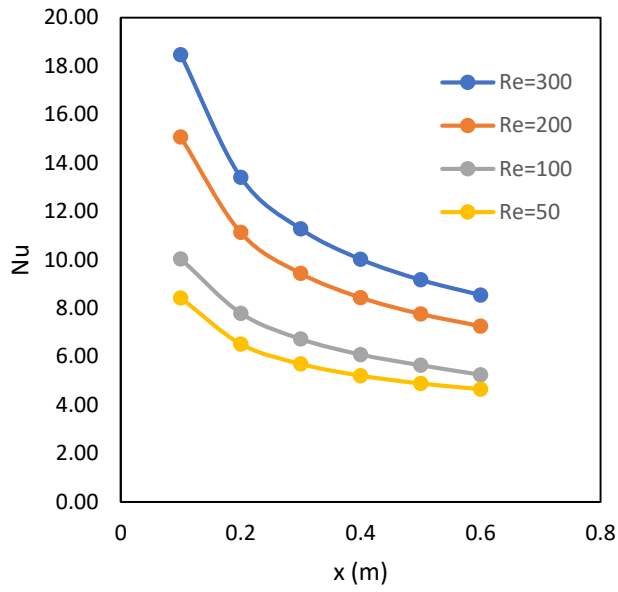


Figure 38: Average Nusselt number as a function of straight length in straight duct geometry

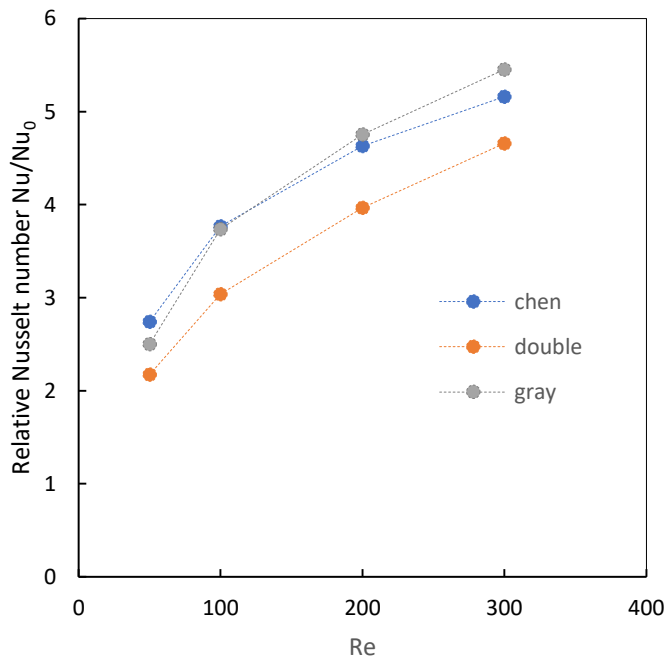


Figure 39: Relative Nusselt number vs. Reynolds number

Figure 39 presents the relative Nusselt number which is ratio of the Nusselt number of SAR geometries to that of the straight duct under similar conditions. It shows the extent of the enhancement that SAR geometries provides over the straight duct for different flow rates. Heat transfer enhancement reaches more than 200% for double, 250% for Gray and 270% for Chen geometries at $Re=50$, the enhancement progresses with the increase of the flow rate to surpass 460% for double, 545% for Gray and 515% for Chen geometry at $Re 300$. The main reason that such improvement is witnessed, is the introduction of chaotic advection. The fluid flow is parallel in straight duct; while it diverges in SAR geometries causing the heated fluid adjacent to the wall to move to colder regions (Bahrani et al, 2016)

It is evident from Figure 39 that as the flow rate rises, Nu increases, hence the best heat transfer is deemed to occur at $Re=300$ in all the 3 SAR configurations under study. Moreover; according to figure 39 for $Re=50$ the highest heat transfer rate is observed in Chen geometry, followed by Gray then the Double geometry, while for $Re 100, 200$ and 300 Gray geometry exhibits the best heat transfer followed by Chen then the double geometry.

The heat transfer is prompted by higher number of splits/recombination in SAR geometries; however beyond a certain flow rate, the advection takes over and the flow becomes dependent on secondary flow and dean vortices.

For the first two flow conditions $Re =50$ and $Re=100$, the reason that Chen geometry shows the highest heat transfer improvement is due to the higher frequency of splitting/recombination, though at $Re= 100$ the thermal performance of Chen and Gray are very close. Chen geometry has 9 elements, the flow in each element split and recombine twice. In comparison Gray geometry has 12 elements in each element the flow split and

recombine only once; while Double geometry has 4 elements in which the flow split twice the recombine twice as well. Hence, the thermal behavior of SAR geometries at $Re=50$ can be attributed to their geometric construction and subsequently the number of splits and recombination that the fluid goes through. This behavior persists at $Re=100$ however; the effect of split recombination ratio diminishes due to the increasing effect of advection.

For the second two flow conditions $Re=200$ and $Re=300$, advection is dominant and the flow is controlled by secondary and Dean vortices. In this case, the heat transfer is dependent on the orientation of the curvature plane and the number of 90 degree bends per unit of developed length. The increased number of 90 degree bends causes more alternating Dean vortices and better heat transfer. This explains why Gray geometry is more favorable than Chen and Double geometries at the studied flow conditions.

To get more insight on how thermal performance relates to power consumption. Nusselt number for all the geometries under study were plotted against the power consumption in Figure 40. It can be deduced from Figure 40 that increasing thermal homogenization requires higher energy consumption. Also, that the straight duct has the worst performance in terms of heat transfer and power dissipation. In addition, the Double SAR reaches its optimal heat transfer at the lowest energy consumption compared to the other geometries. However the Chen and Gray SAR trend lines predicts it can achieve similar heat transfer for similar energy dissipation.

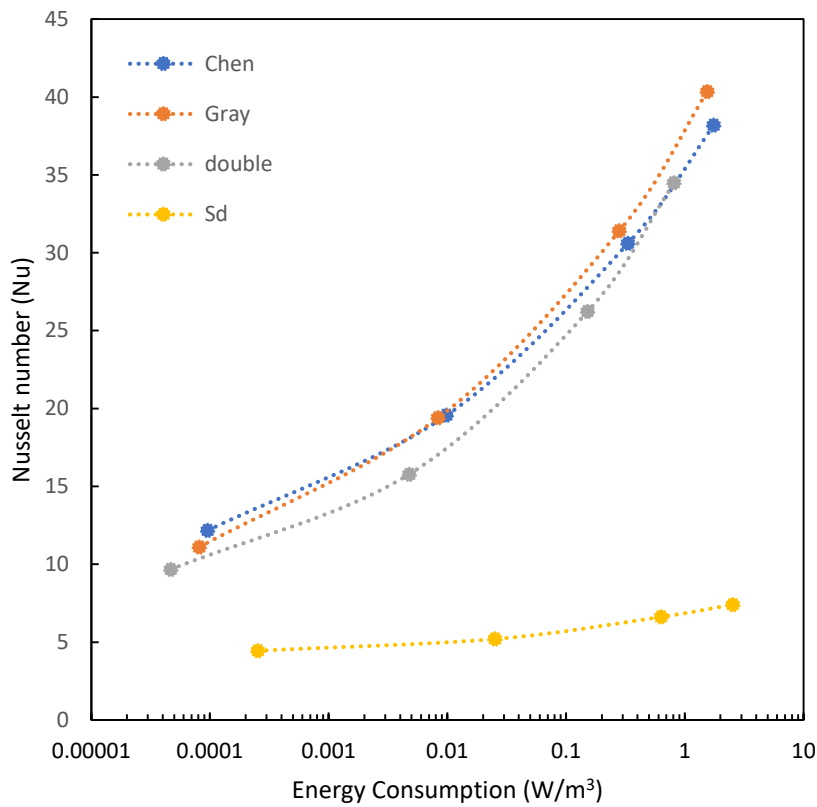


Figure 40: Relation between Nusselt number and Energy Consumption

Characterizing thermal-hydrodynamic performance of the SAR geometries is a necessary step to allow a proper comparative analysis of their overall efficiency and candidacy for industrial applications. Different performance evaluation criteria have been suggested for the purpose of assessing thermal-hydrodynamic performance. One of the most used criterion is the thermal enhancement factor.

By definition the thermal enhancement factor η is defined as the “ratio of the surface heat transfer coefficient (h) in the SAR configuration to that of the duct configuration (h_0), at constant pumping power conditions” (Ghanem et al., 2013b)

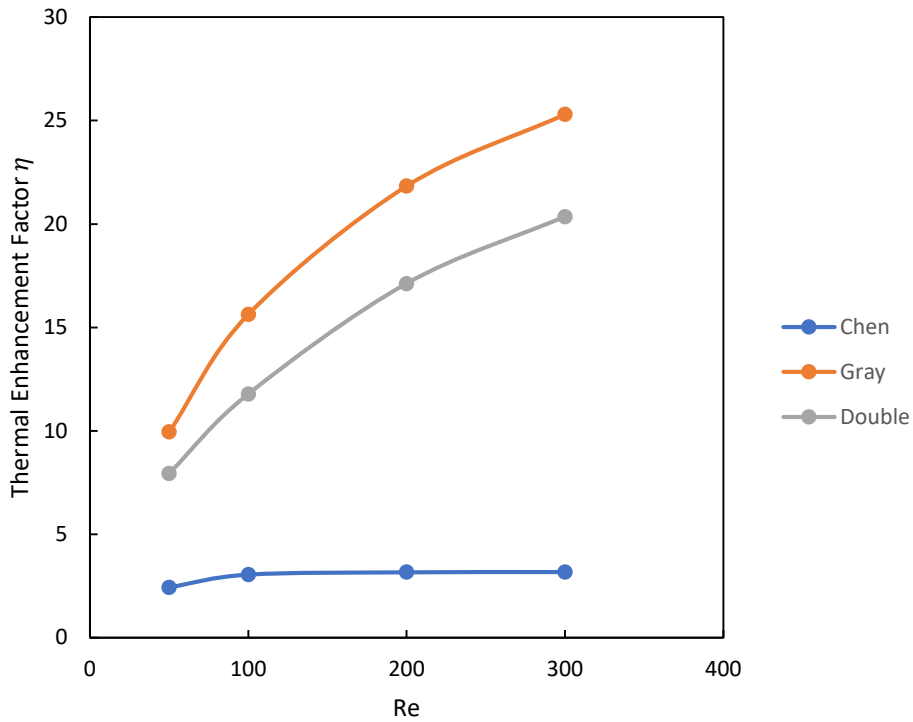


Figure 41: Thermal Enhancement Factor

It is evaluated for the three SAR configurations compared to the straight duct configuration according to the following formula.

$$\eta = \frac{h}{h_0} = \frac{\frac{N_u}{N_{u_0}}}{\left(\frac{f}{f_0}\right)^{1/3}} \quad (30)$$

Figure 41 show the thermal enhancement factor as a function of the flow conditions for the three SAR geometries. Chen geometry showed the worst thermal enhancement compared to Double and Gray. The obtained results in terms of Chen and Gray geometry follow the same patterns as results obtained by Bahrani et al 2019 mentioned in the literature review section of this thesis.

Gray SAR require high energy consumption to attain a mixing efficiency lower than that of Double SAR particularly for $Re < 200$, also Gray and Double SAR have comparable energy performance. Considering these facts, tradeoff between thermal hydraulic, energy consumption and mixing performance show that the Double SAR is a better option than Gray SAR particularly for $Re < 200$, On the other hand, Chen SAR displayed a better mixing performance (by a small margin) compared to the Double SAR, however it lagged behind in terms of its thermal-hydraulic performance, as it was the worst by large margin compared to Gray and Double SAR. Considering these facts as well, a trade of between thermal hydraulic, energy consumption and mixing performance show that the Double geometry is a better option than Chen SAR.

CHAPTER VI

CONCLUSION AND RECOMMENDATIONS

The current study numerically investigated the mixing performance, hydrodynamic and thermal behavior of a novel Double split-and-recombine mixer under different flow conditions. This “Double SAR”, is characterized by a double separation and recombination which multiply the effect of lamination and hence increase mixing efficiency. The mixer performance was assessed and compared to that of the geometries proposed by Gray et al. and Chen and Meiners for $Re= 1, 10, 50, 100, 200, \text{ and } 300$.

The Double geometry showed comparable performance to the Chen geometry and better performance than the Gray geometry for all the flow conditions under study. In addition it has proved to offer better energy requirements as its pressure drop was found to be the lowest among the other SAR geometries and the straight duct. As for its thermal efficiency, the Double geometry showed better overall thermal enhancement than Chen geometry, but it lags behind Gray geometry in that field.

Choosing the design of a multi-functional heat exchanger is highly dependent on its specific use. Considering the tradeoff between mixing efficiency and thermal-hydraulic performance and cost the Double geometry is considered a viable option that combines all these requirements.

This thesis presented an insight on the behavior of viscous fluid in different a Double SAR multifunctional heat exchanger under specific operating conditions. However, there are many areas not covered by this thesis that could benefit from further investigations, mainly covering larger range of fluid flow conditions, introducing a system where a chemical reaction take place and most importantly performing

experimental analysis. In addition, testing a scaled up or scaled down version of the Double SAR designs might provide an insight on its scope of functionality and help determine the optimal its dimensions. Finally, it is recommended to test the Double SAR geometry further for a specific application on future studies is essential to allow us to exploit the full potential of the SAR design.

APPENDIX A

RICHARDSON EXTRAPOLATION

Richardson extrapolation is one of the most widely used methods for mesh sensitivity analysis in CFD since it is capable of enhancing the accuracy of a given computational technique. (Shyy et al., 2002).

The Grid Convergence Index method which is developed based on the Richardson extrapolation is utilized in this research. This method will be applied to one element of each configuration to save computational time. (Celik et al., 2008)

The method of implementation of this procedure is outlined below. It relies on developing three sets of grids the sizes of which are considerably different. For this, the grid refinement ratio between the coarser and the finer grids should be maintained greater than 1.2. Different simulations were then conducted for each grid and the mixing index and pressure drop were calculated.

The grid size h is defined as:

$$h = \left[\frac{1}{N} \sum_{i=1}^N (\Delta V_i) \right]^{1/3} \quad (31)$$

Where: V_i is the volume, and N is the total number of cells used for the computations.

Using the mixing index and pressure drop results from the simulations, the following values are calculated:

The apparent order p :

$$p = \frac{1}{\ln(r_{21})} \left| \ln \left| \frac{\varepsilon_{32}}{\varepsilon_{21}} \right| + q(p) \right| \quad (32)$$

$$q(p) = \ln\left(\frac{r_{21}^p - s}{r_{32}^p - s}\right) \quad (33)$$

$$s = 1 * \text{sgn}\left(\frac{\varepsilon_{32}}{\varepsilon_{21}}\right) \quad (34)$$

Where: $r_{21} = \frac{h_2}{h_1}$, $r_{32} = \frac{h_3}{h_2}$ are the grid refinement ratios such that h_1 is the grid size for the coarser mesh, h_2 is for the finer and h_3 is for the finest.

The difference in the value obtained among the grids in question are defined as $\varepsilon_{32} = \phi_3 - \phi_2$, $\varepsilon_{21} = \phi_2 - \phi_1$, given that ϕ_n is the solution (pressure drop or Cov) of the n^{th} grid.

Next, the extrapolated variables have to be determined using the following equation

$$\phi_{ext}^{21} = \frac{r_{21}^p \phi_1 - \phi_2}{r_{21}^p - 1} \quad (35)$$

Finally, the relative error e_a^{21} and the extrapolated relative error e_{aext}^{21} have to be calculated in order to deduce the grid convergence index:

$$e_a^{21} = \left| \frac{\phi_1 - \phi_2}{\phi_1} \right| \quad (36)$$

$$e_{ext}^{21} = \left| \frac{\phi_{aext}^{21} - \phi_1}{\phi_{aext}^{21}} \right| \quad (37)$$

$$GCI_{fine}^{21} = \frac{1.25 e_a^{21}}{r_{21}^p - 1} \quad (38)$$

Different grids should be developed till reaching appropriate refinement associated with $GCI < 2.5\%$ for each mixer configuration. (Celik et al., 2008).

Table A 1: Richardson extrapolation for straight duct mesh in terms of the head loss

Mesh	Coarse	Intermediate	Finer
	3	2	1
number of cells	1.14×10^6	4.53×10^6	9.73×10^6
h (mm)	0.174	0.110	0.085
ΔP	18930.7	19102.9	19082.9
s			-1
$q(p)$			-0.8778
ϕ_{ext}		19122.0	19075.204
e_a			0.10%
e_{ext}			0.04%
GCI	0.05%		
p	5		

Table A 2: Richardson extrapolation for straight duct mesh in terms of the mixing index

Mesh	Coarser	Intermediate	Finer
	3	2	1
number of cells	1.14×10^6	4.53×10^6	9.73×10^6
h (mm)	0.174	0.110	0.085
Mixing Index	0.135	0.095	0.098
s			-1
$q(p)$			-1.0807
ϕ_{ext}		0.9	0.901
e_a			0.33%
e_{ext}			0.09%
GCI	0.12%		
p	6		

Table A 3: Richardson extrapolation for Gray SAR mesh in terms of the head loss

Mesh	Coarser	Intermediate	Finer
	3	2	1
number of cells	1.73×10^6	3.71×10^6	1.03×10^7
h (mm)	0.151	0.117	0.083
ΔP	24685	24763	24634
s			-1
$q(p)$			0.0646
ϕ_{ext}		24963	24399
e_a			0.52%
e_{ext}			0.96%
GCI	1.19%		

p	1
----------	----------

Table A 4: Richardson extrapolation for Gray SAR geometry in terms of the mixing index

Mesh	Coarser	Intermediate	Finer
	1	2	3
number of cells	1.73×10^6	3.71×10^6	1.03×10^7
h (mm)	0.151	0.117	0.083
Mixing Index	0.9998800	0.9997080	0.99957
s			1
$q(p)$			0.3650
ϕ_{ext}		1.0	0.999
e_a			0.01%
e_{ext}			0.02%
GCI	0.02%		
p	2		

Table A 5: Richardson extrapolation for Double SAR mesh in terms of the head loss

Mesh	Coarser	Intermediate	Finer
	3	2	1
number of cells	7.25×10^5	2.44×10^6	5.03×10^6
h (mm)	0.199	0.133	0.104
ΔP	11829	11817	11808
s			1
$q(p)$			-0.5867
ϕ_{ext}		11781.3	11765.709
e_a			0.07%
e_{ext}			0.36%
GCI	0.45%		
p	1		

Table A 6: Richardson extrapolation for Double SAR mesh in terms of the mixing index

Mesh	Coarser	Intermediate	Finer
	3	2	1
number of cells	7.25×10^5	2.44×10^6	5.03×10^6
h (mm)	0.199	0.133	0.104
Mixing Index	0.9982	0.9978	0.9978
s			1
$q(p)$			-0.9892
ϕ_{ext}		0.99778	0.998

e_a		0.004%
e_{ext}		0.002%
GCI	0.0025%	
p	5	

Table A 7: Richardson extrapolation for Chen SAR mesh in terms of the head loss

Mesh	Coarser	Intermediate	Finer
	1	2	3
number of cells	1.33×10^6	3.04×10^6	1.08×10^7
h (mm)	0.163	0.123	0.081
ΔP	27831.000	28232.000	28581.000
s			1
$q(p)$			0.5587
ϕ_{ext}		28926.9	28926.924
e_a			1.22%
e_{ext}			1.20%
GCI	1.513%		
p	2		

Table A 8: Richardson extrapolation for Chen SAR mesh in terms of the mixing index

Mesh	Coarser	Intermediate	Finer
	3	2	1
number of cells	1.33×10^6	3.04×10^6	1.08×10^7
h (mm)	0.163	0.123	0.081
Mixing Index	0.999999961	0.999999975	0.999999979
s			1
$q(p)$			0.9064
ϕ_{ext}		1.000	1.000
e_a			$4 \times 10^{-7}\%$
e_{ext}			$5 \times 10^{-8}\%$
GCI	0.0000001%		
p	5		

APPENDIX B

MIXING EFFICIENCY AS A FUNCTION OF VARIOUS SAR LENGTHS

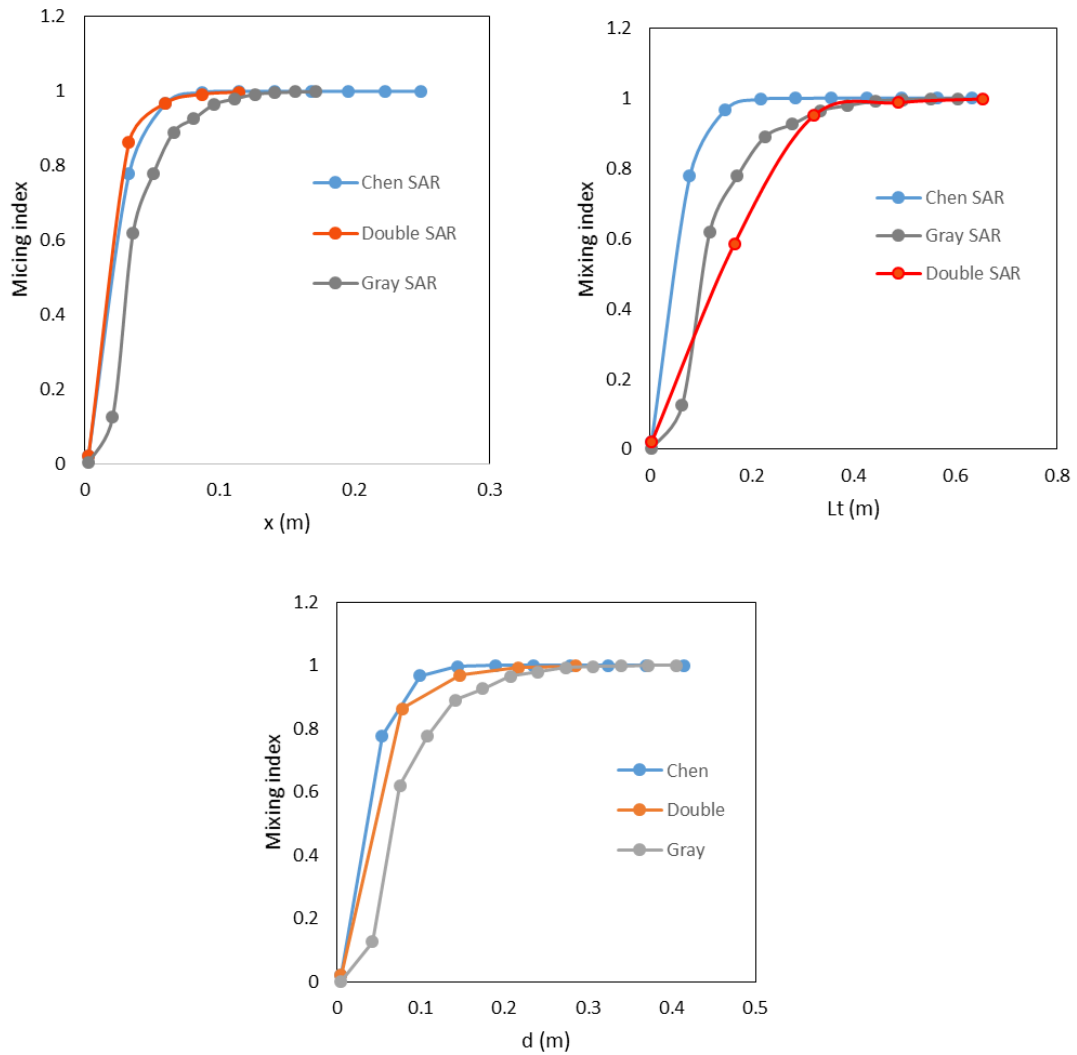


Figure B 1: Variation of mixing index as a function of various SAR length at $Re=300$

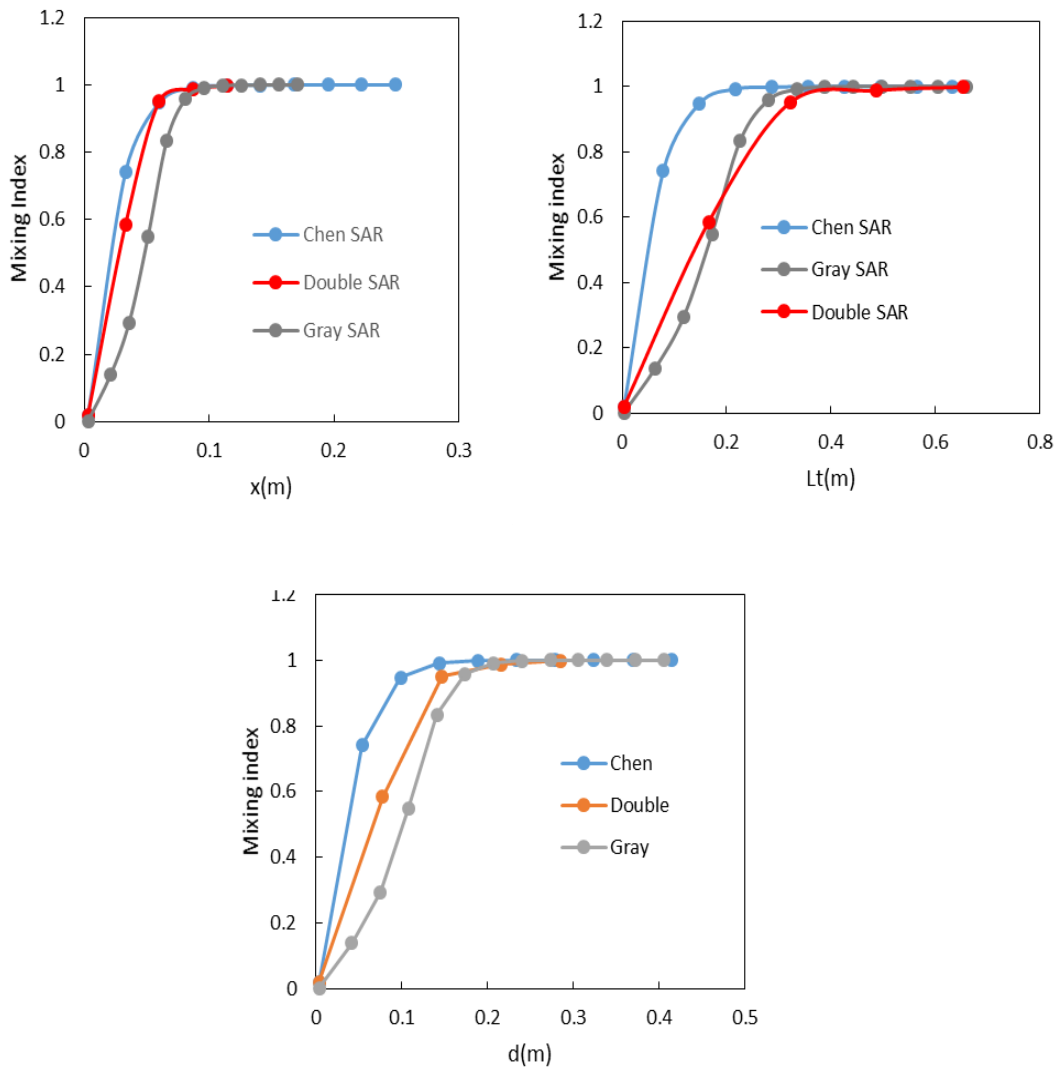


Figure B 2: Variation of mixing index as a function of various SAR length at $Re=200$

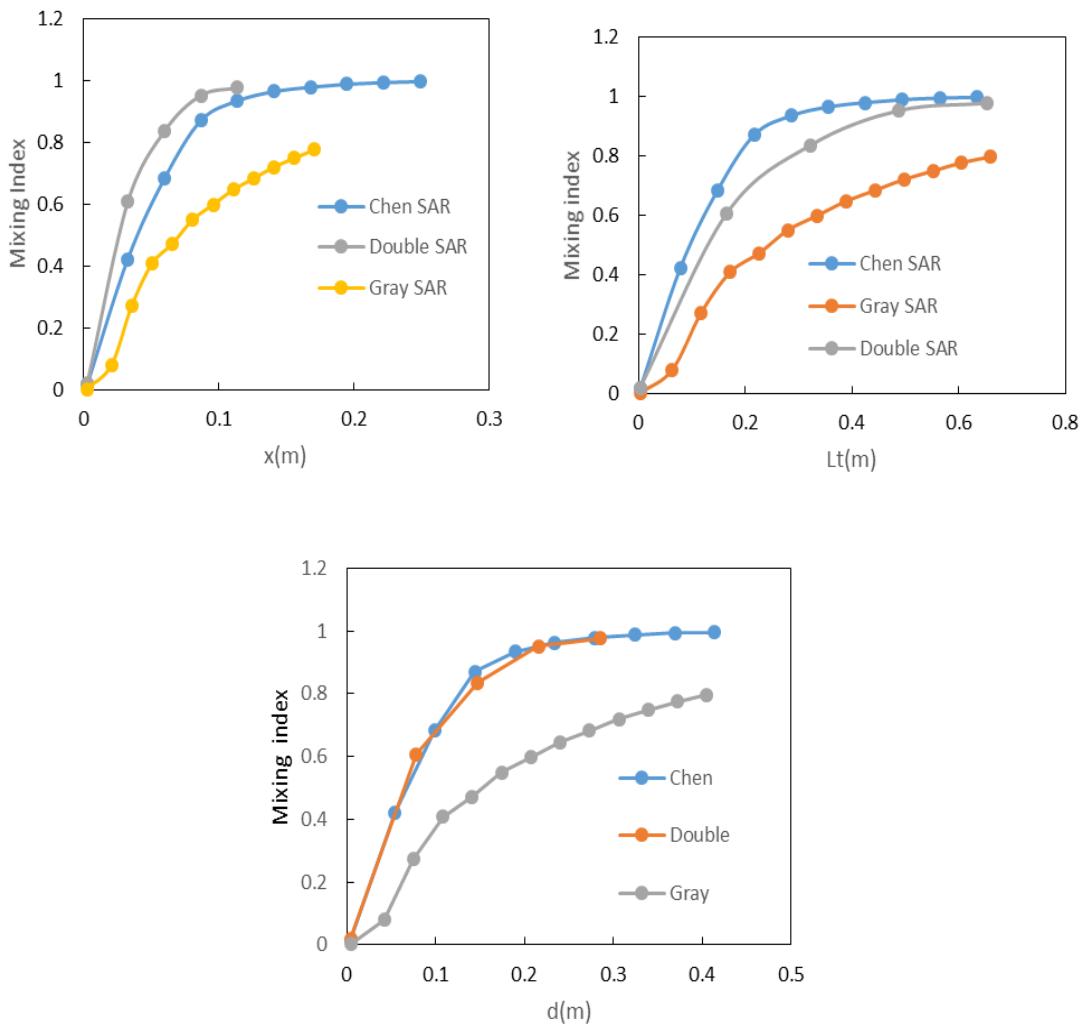


Figure B 3: Variation of mixing index as a function of various SAR length at $Re=100$

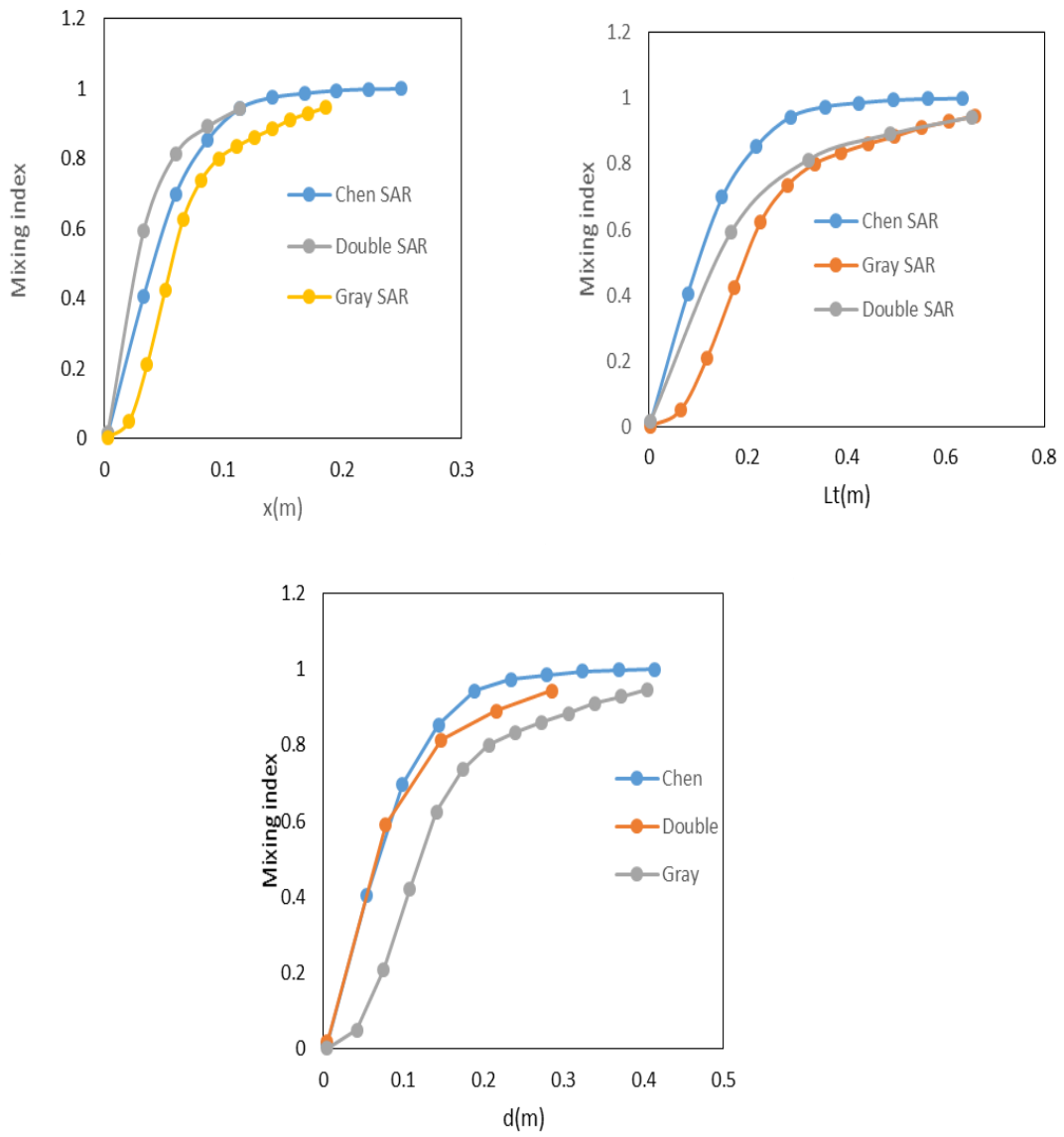


Figure B 4: Variation of mixing index as a function of various SAR length at $Re=50$

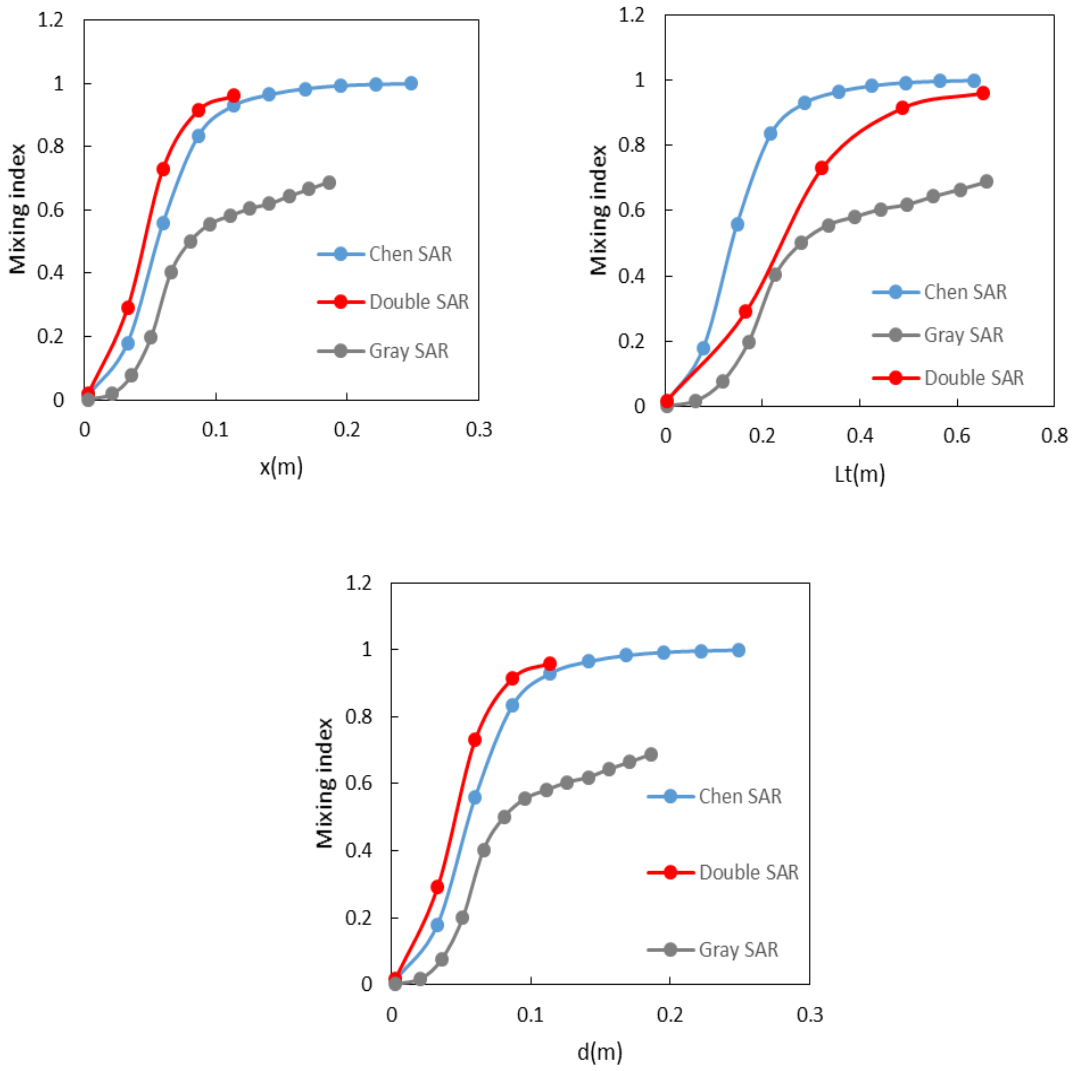


Figure B 5: Variation of mixing index as a function of various SAR length at $Re=50$

REFERENCES

- Afshar Ghotli, R., Abdul Raman, A. A., Ibrahim, S., & Baroutian, S. (2013). Liquid-liquid mixing in stirred vessels: A review. *Chemical Engineering Communications*. doi:10.1080/00986445.2012.717313
- Al-Hassan, T., Habchi, C., Lemenand, T., & Azizi, F. (2021). CFD Simulation of Creeping Flows in a Novel Split-and-Recombine Multifunctional Reactor. *Chemical Engineering and Processing - Process Intensification*, 162, 108353. doi:10.1016/j.cep.2021.108353
- Ali, S. (2015). *Innovative concept of multifunctional heat exchanger/reactor by passive dynamic control using flexible vortex generators*. Mechanics [physics.med-ph]. NNT : 2015VALE0034 . tel-01295212.
- Ansari, M. A., & Kim, K.-Y. (2010). Mixing performance of unbalanced split and recombine micromixers with circular and rhombic sub-channels. *Chemical Engineering Journal*, 162(2), 760-767. doi:10.1016/j.cej.2010.05.068
- ANSYS® (2019). Academic Research Mechanical, Release 19.0, Help System: ANSYS Fluent Theory Guide, chapter 5. Canonsburg, PA: ANSYS, Inc.
- Anxionnaz-Minvielle, Z., Tochon, P., Couturier, R., Magallon, C., Théron, F., Cabassud, M., & Gourdon, C. (2017). Implementation of ‘chaotic’ advection for viscous fluids in heat exchanger/reactors. *Chemical Engineering and Processing: Process Intensification*, 113, 118-127. doi:10.1016/j.cep.2016.07.010
- Aref, H., Blake, J. R., Budišić, M., Cardoso, S. S. S., Cartwright, J. H. E., Clercx, H. J. H., Tuval, I. (2017). Frontiers of chaotic advection. *Reviews of Modern Physics*, 89(2). doi:10.1103/RevModPhys.89.025007

- Bahrani, S., Humberst, L., Osipian, R., Royon, L., Azzouz, K., & Bontemps, A. (2019). How thermally efficient are chaotic advection mixers ? An experimental assessment. *International Journal of Thermal Sciences*, 145. doi:10.1016/j.ijthermalsci.2019.106046
- Bejan, A., & Kraus, A. D. (2003). *Heat Transfer Handbook*. Hopken, New Jersey: John Wiley & Sons, INC.
- Bird, R.B., Stewart W. E., and E.N. Lightfoot. (2007). *Transport Phenomena*: John Wiley & Sons, Inc.
- Boukhalkhal, A. L., Lasbet, Y., Makhlof, M., & Loubar, K. (2017). Numerical study of the chaotic flow in three-dimensional open geometry and its effect on the both fluid mixing and heat performances. *International Journal of Heat and Technology*, 35(1), 1-10.
- Cai, G., Xue, L., Zhang, H., & Lin, J. (2017). A Review on Micromixers. *Micromachines (Basel)*, 8(9). doi:10.3390/mi8090274
- Carrière, P. (2007). On a three-dimensional implementation of the baker's transformation. *Physics of fluids*, 19(11), 118110.
- Celik, I. B., Ghia, U., & Roache, P. J. (2008). Procedure for estimation and reporting of uncertainty due to discretization in {CFD} applications. *Journal of fluids {Engineering-Transactions} of the {ASME}*, 130(7).
- Çengel, Y. A., & Ghajar, A. J. (2011). *Heat and mass transfer: Fundamentals & applications*. New York: McGraw-Hill. .
- Chen, H. M., & Meiners, J. C. (2004). Topologic mixing on a microfluidic chip. *Applied Physics Letters*, 84, 2193-2195.

- Gage, K. S., & Reid, W. H. (2006). The stability of thermally stratified plane Poiseuille flow. *Journal of Fluid Mechanics*, 33(1), 21-32.
doi:10.1017/s0022112068002326
- Garbrecht, O. (2017). *Large eddy simulation of three-dimensional mixed convection on a vertical plate*. (PhD), Rheinisch-Westfälischen Technischen Hochschule Aachen, Germany.
- Ghanem, A., Lemenand, T., Della Valle, D., & Peerhossaini, H. (2013a). *Transport Phenomena in Passively Manipulated Chaotic Flows: Split-and-Recombine Reactors*. Paper presented at the ASME 2013 Fluids Engineering Division Summer Meeting.
- Ghanem, A., Lemenand, T., Della Valle, D., & Peerhossaini, H. (2013b). Optimized Chaotic Heat Exchanger Configurations for Process Industry: A Numerical Study. American Society of Mechanical Engineers, Fluid Engineering Division (Publication), FEDSM , 1. doi:10.1115/FEDSM2013-16115
- Ghanem, A., Lemenand, T., Della Valle, D., & Peerhossaini, H. (2014). Static mixers: Mechanisms, applications, and characterization methods – A review. *Chemical Engineering Research and Design*, 92(2), 205-228.
doi:10.1016/j.cherd.2013.07.013
- Gray, B. L., Jaeggi, D., Mourlas, N. J., van Drieënhuizen, B. P., Williams, K. R., Maluf, N. I., & Kovacs, G. T. A. (1999). Novel interconnection technologies for integrated microfluidic systems1Paper presented as part of the SSAW-98 Workshop.1. *Sensors and Actuators A: Physical*, 77(1), 57-65.
doi:https://doi.org/10.1016/S0924-4247(99)00185-5

- Habchi, C., Lemenand, T., & Azizi, F. (2018). *Mixing Enhancement in a Novel Type of “Split and Recombine” Static Mixer*. Paper presented at the ASME 2018 International Mechanical Engineering Congress and Exposition.
<https://doi.org/10.1115/IMECE2018-88030>
- Habchi, C., Ghanem, A., Lemenand, T., Della Valle, D., & Peerhossaini, H. (2019). Mixing performance in Split-And-Recombine Milli-Static Mixers—A numerical analysis. *Chemical Engineering Research and Design*, *142*, 298-306.
doi:<https://doi.org/10.1016/j.cherd.2018.12.010>
- Hermann, P., Timmermann, J., Hoffmann, M., Schlüter, M., Hofmann, C., Löb, P., & Ziegenbalg, D. (2018). Optimization of a split and recombine micromixer by improved exploitation of secondary flows. *Chemical Engineering Journal*, *334*, 1996-2003. doi:[10.1016/j.cej.2017.11.131](https://doi.org/10.1016/j.cej.2017.11.131)
- Herwig, H. (2016). What exactly is the Nusselt Number in convective heat transfer problems and are there alternatives? *Entropy*, *18*(5), 198.
- Hossain, S., & Kim, K.-Y. (2015). Mixing analysis in a three-dimensional serpentine split-and-recombine micromixer. *Chemical Engineering Research and Design*, *100*, 95-103. doi:[10.1016/j.cherd.2015.05.011](https://doi.org/10.1016/j.cherd.2015.05.011)
- Jarrahi, M., Thermeau, J.-P., & Peerhossaini, H. (2016). Heat Transfer Enhancement in Split and Recombine Flow Configurations: A Numerical and Experimental Study. (50329), V001T005A001. doi:[10.1115/HT2016-7119](https://doi.org/10.1115/HT2016-7119)
- Jegatheeswaran, S., Ein-Mozaffari, F., & Wu, J. (2018). Process intensification in a chaotic SMX static mixer to achieve an energy-efficient mixing operation of non-newtonian fluids. *Chemical Engineering and Processing: Process Intensification*, *124*, 1-10.

- Juraeva, M., & Kang, D. J. (2020). Mixing Performance of a Cross-Channel Split-and-Recombine Micro-Mixer Combined with Mixing Cell. *Micromachines*, 11(7), 685. doi:10.3390/mi11070685
- Konopacki, M., Kordas, M., Fijałkowski, K., & Rakoczy, R. (2015). Computational Fluid Dynamics and Experimental Studies of a New Mixing Element in a Static Mixer as a Heat Exchanger. *Chemical and Process Engineering*, 36(1), 59-72. doi:10.1515/cpe-2015-0005
- Khaydarov, V., Borovinskaya, E., & Reschetilowski, W. (2018). Numerical and Experimental Investigations of a Micromixer with Chicane Mixing Geometry. *Applied Sciences*, 8, 2458. doi:10.3390/app8122458
- Mangani, L., Sanz, W., & Darwish, M. (2016). *Comparing the performance and accuracy of a pressure based and a density-based coupled solver*. Paper presented at the 16th International Symposium on Transport Phenomena and Dynamics of Rotating Machinery, Honolulu, United States.
- Meijer, H. E. H., Singh, M. K., Kang, T. G., den Toonder, J. M. J., & Anderson, P. D. (2009). Passive and Active Mixing in Microfluidic Devices. *Macromolecular Symposia*, 279(1), 201-209. doi:10.1002/masy.200950530
- Mosorov, V. (2015). Applications of tomography in reaction engineering (mixing process). 509-528. doi:10.1016/b978-1-78242-118-4.00019-8
- Nguyen, N.-T. (2012). Micromixers based on chaotic advection. 195-238. doi:10.1016/b978-1-4377-3520-8.00006-1
- Ohkawa, K., Nakamoto, T., Izuka, Y., Hirata, Y., & Inoue, Y. (2008). Flow and mixing characteristics of σ -type plate static mixer with splitting and inverse recombination. *Chemical Engineering Research and Design*, 86(12), 1447-1453.

- Rashidi, M. M., Ferdows, M., Parsa, A. B., & Abelman, S. (2014). *MHD natural convection with convective surface boundary condition over a flat plate*. Paper presented at the Abstract and Applied Analysis.
- Shah, N., Animasaun, I., Ibraheem, R., Babatunde, H., Sandeep, D. N., & Pop, I. (2017). Scrutinization of the effects of Grashof number on the flow of different fluids driven by convection over various surfaces. *Journal of Molecular Liquids*, 249, 980-990. doi:10.1016/j.molliq.2017.11.042
- Shyy, W., Garbey, M., Appukuttan, A., & Wu, J. (2002). EVALUATION OF RICHARDSON EXTRAPOLATION IN COMPUTATIONAL FLUID DYNAMICS. *Numerical Heat Transfer, Part B: Fundamentals*, 41(2), 139-164. doi:10.1080/104077902317240058
- Singh, A., Harinadha, G., Kishore, N., Barua, P., Jain, T., & Joshi, P. (2015). Mixed Convective Heat Transfer Phenomena of Circular Cylinders to Non-Newtonian Nanofluids Flowing Upward. *Procedia Engineering*, 127. doi:10.1016/j.proeng.2015.11.434
- Viktorov, V., Mahmud, M. R., & Carmen, V. (2015). Numerical Analysis of Fluid Mixing in Three Split and Recombine Micromixers at Different Inlets Flow Rate Ratio.
- Xing, T., & Stern, F. (2010). Factors of Safety for Richardson Extrapolation. *Journal of Fluids Engineering*, 132(6). doi:10.1115/1.4001771